



LAWRENCE
LIVERMORE
NATIONAL
LABORATORY

3D Vectorial Time Domain Computational Integrated Photonics

J. S. Kallman, T. C. Bond, J. M. Koning, M. L.
Stowell

February 26, 2007

Disclaimer

This document was prepared as an account of work sponsored by an agency of the United States Government. Neither the United States Government nor the University of California nor any of their employees, makes any warranty, express or implied, or assumes any legal liability or responsibility for the accuracy, completeness, or usefulness of any information, apparatus, product, or process disclosed, or represents that its use would not infringe privately owned rights. Reference herein to any specific commercial product, process, or service by trade name, trademark, manufacturer, or otherwise, does not necessarily constitute or imply its endorsement, recommendation, or favoring by the United States Government or the University of California. The views and opinions of authors expressed herein do not necessarily state or reflect those of the United States Government or the University of California, and shall not be used for advertising or product endorsement purposes.

This work was performed under the auspices of the U.S. Department of Energy by University of California, Lawrence Livermore National Laboratory under Contract W-7405-Eng-48.

FY06 LDRD Final Report
3D Vectorial Time Domain Computational Integrated Photonics
LDRD Project Tracking Code: 04-ERD-004
Jeffrey S. Kallman, Principal Investigator
Tiziana C. Bond, Co-Investigator
Joseph M. Koning, Co-Investigator
Mark L. Stowell, Co-Investigator

Disclaimer

This document was prepared as an account of work sponsored by an agency of the United States Government. Neither the United States Government nor the University of California nor any of their employees, makes any warranty, express or implied, or assumes any legal liability or responsibility for the accuracy, completeness, or usefulness of any information, apparatus, product, or process disclosed, or represents that its use would not infringe privately owned rights. Reference herein to any specific commercial product, process, or service by trade name, trademark, manufacturer, or otherwise, does not necessarily constitute or imply its endorsement, recommendation, or favoring by the United States Government or the University of California. The views and opinions of authors expressed herein do not necessarily state or reflect those of the United States Government or the University of California, and shall not be used for advertising or product endorsement purposes.

LDRD Auspices Statement

This work was performed under the auspices of the U. S. Department of Energy (DOE) by the University of California, Lawrence Livermore National Laboratory (LLNL) under Contract No. W-7405-Eng-48. The project 04-ERD-004 was funded by the Laboratory Directed Research and Development Program at LLNL.

Introduction/Background

The design of integrated photonic structures poses considerable challenges. 3D-Time-Domain design tools are fundamental in enabling technologies such as all-optical logic, photonic bandgap sensors, THz imaging, and fast radiation diagnostics.

Such technologies are essential to LLNL and WFO sponsors for a broad range of applications: encryption for communications and surveillance sensors (NSA, NAI and I-DIV/PAT); high density optical interconnects for high-performance computing (ASCI); high-bandwidth instrumentation for NIF diagnostics; micro-sensor development for weapon miniaturization within the Stockpile Stewardship and DNT programs; and applications within HSO for CBNP detection devices.

While there exist a number of photonics simulation tools on the market, they primarily model devices of interest to the communications industry. We saw the need to extend our previous software to match the Laboratory's unique emerging needs. These include modeling novel material effects (such as those of radiation induced carrier concentrations on refractive index) and device configurations (RadTracker bulk optics with radiation induced details, Optical Logic edge emitting lasers with lateral optical inputs). In addition we foresaw significant advantages to expanding our own internal simulation codes: parallel supercomputing could be incorporated from the start, and the simulation source code would be accessible for modification and extension.

This work addressed Engineering's Simulation Technology Focus Area, specifically photonics. Problems addressed from the Engineering roadmap of the time included modeling the Auston switch (an important THz source/receiver), modeling Vertical Cavity Surface Emitting Lasers (VCSELs, which had been envisioned as part of fast radiation sensors), and multi-scale modeling of optical systems (for a variety of applications).

We proposed to develop novel techniques to numerically solve the 3D multi-scale propagation problem for both the microchip laser logic devices as well as devices characterized by electromagnetic (EM) propagation in nonlinear materials with time-varying parameters. The deliverables for this project were extended versions of the laser logic device code **Quench2D** and the EM propagation code **EMSolve** with new modules containing the novel solutions incorporated by taking advantage of the existing software interface and structured computational modules.

Our approach was multi-faceted since no single methodology can always satisfy the tradeoff between model runtime and accuracy requirements. We divided the problems to be solved into two main categories: those that required *Full Wave Methods* and those that could be modeled using *Approximate Methods*. Full Wave techniques are useful in situations where Maxwell's equations are not separable (or the problem is small in space and time), while approximate techniques can treat many of the remaining cases.

For both approaches we started by enhancing existing software. **EMSolve** began as a parallel finite-element time-domain (FETD) code for solving the full-wave Maxwell's equations. This code had been successfully used for optical simulations such as pulse propagation in bent step-index fibers, wave propagation in PBG fibers and bends, and optical trapping of dielectric microspheres.

The main research thrusts for EMSolve were the incorporation of carrier dynamics, time-varying non-linear material models, gain and spontaneous emission, and multi-scale

simulation. At the beginning of this project, EMSolve supported only linear permittivity, permeability, and conductivity. The goal was a code capable of full-wave 3D simulations of complex non-linear optical devices such as VCSEL's, photonic bandgap devices, and THz sources/receivers.

Carriers can be generated either electrically or optically, and have profound effects on the response of semiconductor materials to a voltage or an optical signal. If the carrier density is high enough, photons can be generated (either randomly as spontaneous emission or by stimulation to provide gain). The incorporation of carrier dynamics, time varying material models, and gain and spontaneous emission were essential to the modeling of semiconductor optical devices. Previous research had been performed on incorporating non-linear material models into finite-different time-domain (FDTD) codes, and this was a starting point for our research [1,2,3,4,5,6].

Quench2D began as a semiconductor laser simulator. It allowed propagation within photonic structures characterized by loss and/or gain by including the interaction with the material through the coupled carrier rate equations [7,8,9]. It is based on the Beam Propagation Method (BPM), which relies on the paraxial approximation of Maxwell's equations allowing the separation of variables. The code had successfully simulated several edge-emitting lasers (EELs) and all-optical digital logic gates in which the devices' cross-section is approximated by an equivalent 1D waveguide.

The main research thrust for Quench2D was extending the technique to a full 3D BPM model and incorporating polarization effects. Our work focused on extending Quench2D to a hybrid 3D version, combining a 2D transverse finite element solver with a vector BPM.

Quench2D and **EMSolve**'s upgrades were complementary efforts. The former to handle larger devices, i.e. edge emitting lasers and amplifiers or tapers and directional couplers, because it is less time and memory intensive, the latter to be used for those configurations where the separation of variables is not allowed. For fully 3D cases (VCSELs, and PBGs) EMSolve was critical since it is very general but also much more time and memory consuming and therefore useful for smaller devices (less than a few tens of cubic wavelength).

Research Activities

EMSolve Computer Science Research

The major contributions of this project to the computer science behind EMSolve were research into: virtual matrices, computation on submeshes, wedge products, and time varying constitutive parameters.

Virtual Matrices

For EMSolve we typically assemble global mass and stiffness matrices so that we can use the Hypr solver library. For large problems these matrices can become extremely

large. This means that EMSolve is often more constrained by memory usage than by cpu usage.

To avoid this problem many large finite element codes choose not to assemble these matrices. Instead they perform matrix-vector multiplies element by element. This choice requires them to use other solvers, perhaps even requiring that they write their own. It can also mean computing local mass and stiffness matrices each time that they are needed (which can be very computationally expensive). For problems where the mesh moves this is a necessary expense. For EMSolve the matrices rarely change so we would prefer to avoid recomputing them.

It should be noted that the presence of time varying material properties can also necessitate recomputing the matrices. One of the major goals of this work is to handle time varying material coefficients as efficiently as possible. While the implementation we used for testing and evaluation did not support material coefficients, the modifications to do so are straightforward.

Many of the devices modeled in the LDRD can be described using highly structured meshes (i.e. meshes which contain a large number of identically shaped elements). In this special case there is a nice compromise between forming global matrices and computing them element by element; compute and cache one local matrix for each group of identical elements and cache the data used to map global degrees of freedom to element based degrees of freedom. This scheme, which we refer to as a “Virtual Matrix” scheme, was implemented and incorporated in EMSolve.

Sub-meshes

One problem that had to be addressed during this LDRD was the interaction of different physics at different time scales, in different regions of the computational domain. This last issue was addressed by implementing what we call the “Sub-Mesh” software. The idea is straightforward although the implementation, as always, was more complicated. We start with a mesh defined on our entire computational domain. We then duplicate the small portion of that mesh which covers the sub-domain wherein some other physics is taking place. In our case the full computational domain consisted of a large volume through which electromagnetic waves would propagate, reflect, etc. The sub-domain was a much smaller volume of semiconductor in which positive and negative charge densities would flow subject to an advection-diffusion equation. Once the sub-mesh itself was defined on the semiconductor region we created linear operators to map the electromagnetic waves onto the semiconductor mesh and a similar operator to map the charge densities back to elements in the full mesh. This allows us to easily run coupled simulations side-by-side in a single code.

Wedge-Products

EMSolve is based on the concept of discrete differential forms. These distinguish between ordinary scalar fields and density fields as well as between vector fields

and pseudo-vector fields (or fluxes.) These distinctions allow us to more accurately reproduce field discontinuities at material interfaces, compute derivative operators more robustly, write conservative time stepping algorithms, etc. They also require more care when computing scalar products, vector cross products, and dot products. In the language of differential forms these products are special cases of what are called "Wedge products".

A Wedge product, denoted $\alpha \wedge \beta$, is the exterior product of two differential forms. The wedge product of a p-form and a q-form is a p+q-form. Furthermore, since a p-form can be represented as an antisymmetric tensor of rank p, $\alpha \wedge \beta = 0$ if $p+q > n$ where α and β are p and q-forms and n is the dimension of the space in which the differential forms are defined.

The wedge product is bilinear and associative but not necessarily commutative. Specifically,

$$\begin{aligned}(a_1\alpha_1 + a_2\alpha_2) \wedge \beta &= a_1(\alpha_1 \wedge \beta) + a_2(\alpha_2 \wedge \beta) \\ \alpha \wedge (b_1\beta_1 + b_2\beta_2) &= b_1(\alpha \wedge \beta_1) + b_2(\alpha \wedge \beta_2) \\ (\alpha \wedge \beta) \wedge \gamma &= \alpha \wedge (\beta \wedge \gamma) \\ \alpha \wedge \beta &= (-1)^{pq} \beta \wedge \alpha\end{aligned}$$

where α is a p-form, β is a q-form, and a_1, a_2, b_1 , and b_2 are scalars.

In \mathcal{R}^3 there are six unique wedge products (the subscripts denote the type of p-form):

Wedge Product	Action	Mathematical Formulation
$\alpha_0 \wedge \beta_0 = \gamma_0$	Scalar Multiplication	$\gamma_0 = \alpha_0 * \beta_0$
$\alpha_0 \wedge \beta_1 = \gamma_1$	Scalar Multiplication	$\gamma_1 = \alpha_0 * \beta_1$
$\alpha_0 \wedge \beta_2 = \gamma_2$	Scalar Multiplication	$\gamma_2 = \alpha_0 * \beta_2$
$\alpha_0 \wedge \beta_3 = \gamma_3$	Scalar Multiplication	$\gamma_3 = \alpha_0 * \beta_3$
$\alpha_1 \wedge \beta_1 = \gamma_2$	Vector Cross Product	$\gamma_2 = \alpha_1 \times \beta_1$
$\alpha_1 \wedge \beta_2 = \gamma_3$	Scalar Dot Product	$\gamma_3 = \alpha_1 \cdot \beta_2$

The first four are simply equivalent to scalar multiplication. The wedge product of two 1-forms is their cross product. The wedge product of a 1-form and a 2-form is their dot product.

Time Varying Constitutive Parameters

Material coefficients are typically incorporated into mass or stiffness matrices when these are computed. The coefficients may be scalar or tensor valued constants or functions. For the applications of interest to this project only scalar valued coefficients are relevant. Scalar coefficients simplify the computation of the integrals involved in computing these matrices but these computations are still very time consuming and we do not want to repeat this effort at each time step.

One alternative is to compute local matrices for each element without any material coefficient. Then make the simplifying assumption that the coefficient is essentially constant within each element. Now the local matrices can be scaled by these constants before use. This alternative fits very well into the virtual matrix scheme. Recall that this scheme involves performing small matrix-vector multiplies $b = Ax$ separately for each element and combining the results. To incorporate material coefficients into this scheme we simply compute scaled matrix-vector multiplies $b = \alpha Ax$ where the scale factors are, of course, given by the values of the material coefficient in each element. To implement this we provide one additional vector of coefficient values to the virtual matrix. Updating this vector at each time step is then equivalent to recomputing the entire matrix using new coefficient values. This alternative was chosen to handle the time-varying permittivity and electric conductivity in our full wave electromagnetics simulation codes.

Another alternative is to represent the material coefficient as a 0-Form scalar field and use the wedge product to multiply this quantity onto other field vectors. This alternative produces a coefficient which can vary within elements and remains continuous at element interfaces. In general continuity may not be desirable as it would tend to smear out any discontinuities in the coefficient. It can also be more expensive to compute because wedge products typically require one or two matrix-vector

multiplications when they are applied. This alternative was chosen to implement the coefficients α and β in the scalar advection-diffusion code. The reason for this is two-fold. First, these coefficients should be continuous throughout the computational domain so 0-Forms are appropriate. Furthermore writing a formulation which has no material coefficients in the matrices makes it much more simple to reuse those matrices and this can reduce memory requirements significantly.

EMSolve Electromagnetic Field and Carrier Dynamics Research

The major contributions of this project to the physics of EMSolve were research into: coupling carrier dynamics with electromagnetics, incorporating nonlinear materials using time varying polarization equations, and adding the capability to project solutions into the far field.

Coupling Carrier Dynamics and Electromagnetics

The coupling of carrier diffusion integrators and electrodynamic solvers was researched and implemented for photonic integrated circuit simulations. A drift diffusion solver calculates the electron and hole densities for a given semiconductor device. These densities are used to determine a current density source for the electrodynamic equations. In order to make this coupled system more efficient a submesh object was implemented to separate the carrier dynamics simulation grid from the full structure. In addition, efficient vector operations and finite element library optimizations were implemented providing a 12x speed improvement. This advanced model was used to study and design THz photo-conductive (Auston switch) antennas, and summarized in 2006 APS IEEE Proceedings [12].

The nonlinearity in the code for Auston switch modeling is implemented using the drift diffusion equations. These equations model the concentrations of holes and electrons within the semiconductor material. The motion of the holes and electrons includes drift due to an applied electric field and the diffusion of the carriers through the material. The semiconductor material can be coupled to separate regions of different materials including dielectrics with no carriers present using the submesh feature described previously. The coupled electrodynamic equations and carrier dynamics equations are solved in an iterative fashion. The electric field from the electrodynamic equations is supplied to the drift diffusion equations for the motion of the holes and electrons. The location of these carrier densities are used to determine the current density in the material. This current density is then used as a source in the full three-dimensional, vectorial electrodynamic equations. The equations are solved iteratively until convergence.

Addition of Nonlinear Effects

The second main research topic for EMSolve electrodynamic was the addition of nonlinear effects through the auxiliary differential equation (ADE) solution of a time-varying polarization equation. The time-varying polarization can be used to model the

gain and absorption of electromagnetic fields in laser materials. This additional solver provides the polarization to the electrodynamics equations, which includes time-varying material parameters and gain/absorption of the medium. In the code both a two-level and four-level atomic system for a two-electron model of the lasing medium were researched and implemented. These solvers were based on auxiliary differential equation methods developed for finite-difference time domain (FDTD) codes [17]-[19]. The net polarization of the medium is determined through the classical electron oscillator model also called the Lorenz model [20]. For each of two interacting electrons a simplified quantized model with two or four energy is used. The two and four level systems determine the Polarization in the medium through the solution of coupled rate equations. The coupled rate equations and Pauli exclusion principle determine the transitions between the different energy levels.

In the code transitions are defined by two coupled dipole oscillators. If the levels are numbered in increasing energy from 0 to 3, then one dipole has levels corresponding to 1 and 2 while the other dipole corresponds to levels 0 and 3. Each of the dipoles yields a governing oscillator equation for the polarization. The combination of these two equations yields the total polarization. This differs from the second type of ADE solver that does include the two and four level models but does not include the Pauli exclusion principle.

Far Field Projection

The far field solver uses an efficient inline discrete Fourier transform to determine the electric and magnetic current densities on a given surface within the simulation domain. The far-field interface uses the same mesh and surface definition as the main simulation code. The efficient inline nature of the code allows several frequencies in the discrete Fourier transform to be calculated at once. A running sum method is used to calculate the potentials and current densities on the surface and maintains a valid set even for truncated simulation runs. A second, post processing, program is then used to calculate the far field for a given set of angles. This allows a general analysis to be performed without rerunning the entire simulation.

Quench3d Vectorial Photonic Design Research

The major contributions of this project to extending our semiconductor laser modeling tools were: extension of Quench2D to 3D, upgrading the scalar solver with a vector solver, and improving the temporal aspects of the code. Incidentally we coupled the decay-diffusion results from the EMSolve code to a 3D BPM code to enhance our utility to the RadTracker project.

The primary effort in upgrading the scalar Quench2D code to operate in 3D was in parallelizing the code. This involved some research into optimal ways to partition the problem, but once those decisions had been made the coding was fairly straightforward. Significantly more effort was required to upgrade the code to using a vector solver. We eventually settled on a solver based on the work of Shultz [10] (which provided a finite element based monochromatic vector beam propagation code) and Feng [11] (which

converted the solver from a monochromatic beam propagation code to a narrow bandwidth beam propagation code). Although the Feng method of extending the bandwidth of the simulation was more accurate than the method we were using previously, it placed restrictions on the parallelization of the code. This version of the software is currently running on a serial platform. We modified this system to deal with time varying constitutive parameters as well as second order nonlinear effects (such as self-focusing). We also researched coupling a subgrid carrier diffusion solver to the system to allow modeling of semiconductor lasers with polarization effects.

QED for Semiconductor Material Modeling Research

A tool for modeling the dependence of gain and refractive index on wavelength and carrier density was developed for analyzing nonlinear effects in both heterostructure and quantum well (QW) semiconductor devices. Bandfilling, bandgap shrinkage, free carrier, and excitonic absorption effects were evaluated, and results were verified against those found in the literature. The model can be used in understanding the nonlinear characteristics of semiconductors under x-ray radiation, aiding in the design of sensitive high-speed radiation detection devices.

Heterostructures

The main carrier related effects that induce changes of the absorption (gain) in bulk semiconductor material are bandgap shrinkage, bandfilling, free carrier absorption. Excitonic saturation exists but the excitonic feature is not very strong thus the effect is small. In bandgap shrinkage, injected electrons occupy states at the bottom of the conduction band, resulting in a lowering of the conduction band edge (blue shift of the spectrum). The valence band edge similarly increases due to the presence of holes. The result is a shrinking of the gap between the bands. For bandfilling to occur in injected semiconductors, the density of states must be sufficiently low such that a small number of carriers can fill the bands. The effective bandgap increases, because electrons in the valence band require more energy to be excited into the conduction band. (red shift of the spectrum or of the photoluminescence or laser emission wavelength). A free carrier can absorb a photon and move to a higher energy state within a band. This intraband absorption is sometimes called the “plasma effect.”

Quantum Wells

Devices often use quantum wells (QWs) to maximize the changes in absorption. A QW consist of a region with smaller bandgap embedded between two barriers, regions with larger bandgap. The structures we modeled were unstrained, undoped single quantum wells. The carriers are assumed to be injected into the quantum well from the ends of the barrier region. Intermixing and excitonic effects (greatly enhanced here due to the engineered confinement of carriers) are included for modeling the properties of actual devices.

Results/Technical Outcome

EMSolve Computer Science Results

Virtual Matrices

Our meshes are split into groups of elements having the same topology. When using virtual matrices we also require that they have the same size and shape. With this assumption we can compute one local mass or stiffness matrix for each group of elements and cache these. We then construct a mapping matrix which can be multiplied onto our vector of global degrees of freedom. The resulting vector consists of element based degrees of freedom (DOFs) stored in contiguous memory and properly ordered. The length of this vector will then be equal to the number of local elements times the number of DOFs per element. With these larger vectors of DOFs we can now perform element by element matrix-vector multiplication quite efficiently. Storing the results in a similar long vector. Finally we use the transpose of our mapping matrix to recombine the element based results into a global DOF vector.

Depending on the topology and the pattern of shared element DOFs the length of these internal vectors can be in the neighborhood of four times larger than the number of local DOFs. The mapping matrix will have only one non-zero per row so it is of a similar size. The results are quite promising. For first order basis functions the memory usage is cut by more than a factor of three. For second order bases the factor is over 17. Finally, for cubic bases the memory usage drops by nearly 50 times.

The conclusions are quite clear. If memory efficiency is a driving factor then virtual matrices are highly advisable. With lowest order basis functions this choice incurs a performance drop of 20 to 30% but this may be worthwhile. Furthermore, if the use of high order bases is possible (e.g. if the solution has no singularities) then virtual matrices produce even more significant memory savings along with a considerable performance gain.

The development of the virtual matrix code and its incorporation into the EMSolve suite of codes may be one of the most valuable software enhancements of this LDRD. For the class of problems where this can be utilized it has already provided us with a means to run larger problems than we could have before. What's more these problems require fewer processors and less CPU time.

Sub-meshes

Once code was available to generate sub-meshes and the necessary mapping matrices it was a simple matter to develop rudimentary multi-physics codes for our class of problems. This scheme may seem ad-hoc or even trivial but it had the advantage of being relatively simple to implement and quite flexible. This scheme also allowed us to take full advantage of the rather sizable amount of code that we already had. This leveraging of existing code enabled us to develop full multi-physics codes in a matter of days by reusing separate applications which had taken weeks or months to develop. This Sub-

Mesh software has already been incorporated back into some of our other applications where it is being used, for example, to improve the modeling of electromagnetic fields in the presence of a variety of conducting and non-conducting materials.

Wedge-Products

The wedge product code developed for this project is enormously powerful. It provides an efficient and consistent method for computing scalar products, cross products, and dot products of our field quantities. These in turn allow us to accurately compute quite a variety of relevant auxiliary fields such as the electromagnetic energy density, Joule heating, the Poynting vector, etc.

EMSolve Electromagnetic Field and Carrier Dynamics Research

The *EMSolve* code has been enhanced to enable electrodynamic simulations with nonlinear materials. In the beginning of the LDRD research an initial thrust area for Terahertz photoconductive devices was targeted. This Terahertz thrust area initiated the first major nonlinear material implementation. The main simulation for the Terahertz thrust area is the Auston switch device. This device is an electrophotonic device that involves a semiconductor device with a large bias electric field and an antenna for the resonant output. The coupled electrodynamic-semiconductor device requires a solver for the electron and hole densities in the device implemented through a drift-diffusion solver. The simulation of arrays of Auston switches was presented at the 2006 IEEE APS meeting [12].

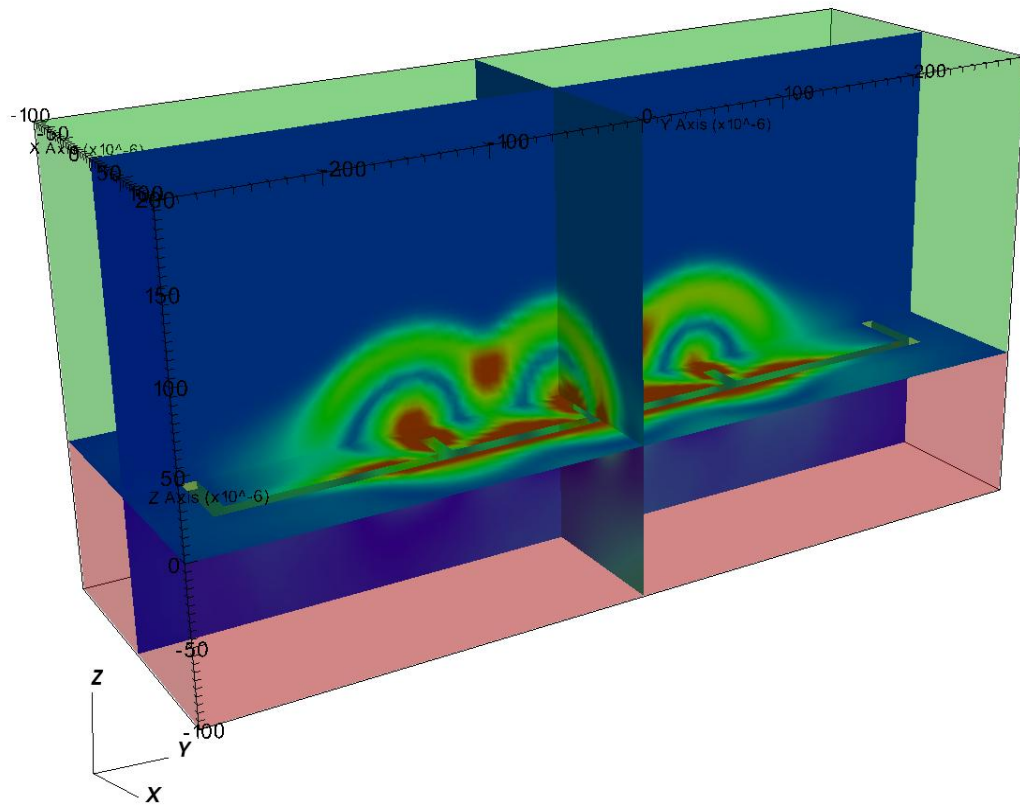


Figure 1: This figure shows the electric field magnitude for the Auston switch device at $t=0.8$ picoseconds. Each of the three antennas (at the centers of the three domes of electric field) in the picture is excited with varying delay.

In a separate integrator a polarization model was implemented using both 2 and 4-level absorption/gain models with and without the Pauli exclusion principle. The figure below shows the linear and nonlinear response to a medium using the two-level integrator. This simulation was a full three-dimensional domain with absorbing medium. For the linear regime with a 100 V/m field the population density remains constant. At this field level the medium acts like a linear absorber. The plot for the non-linear field $5e9 \text{ V/m}$ clearly show the Rabi-flopping phenomenon.

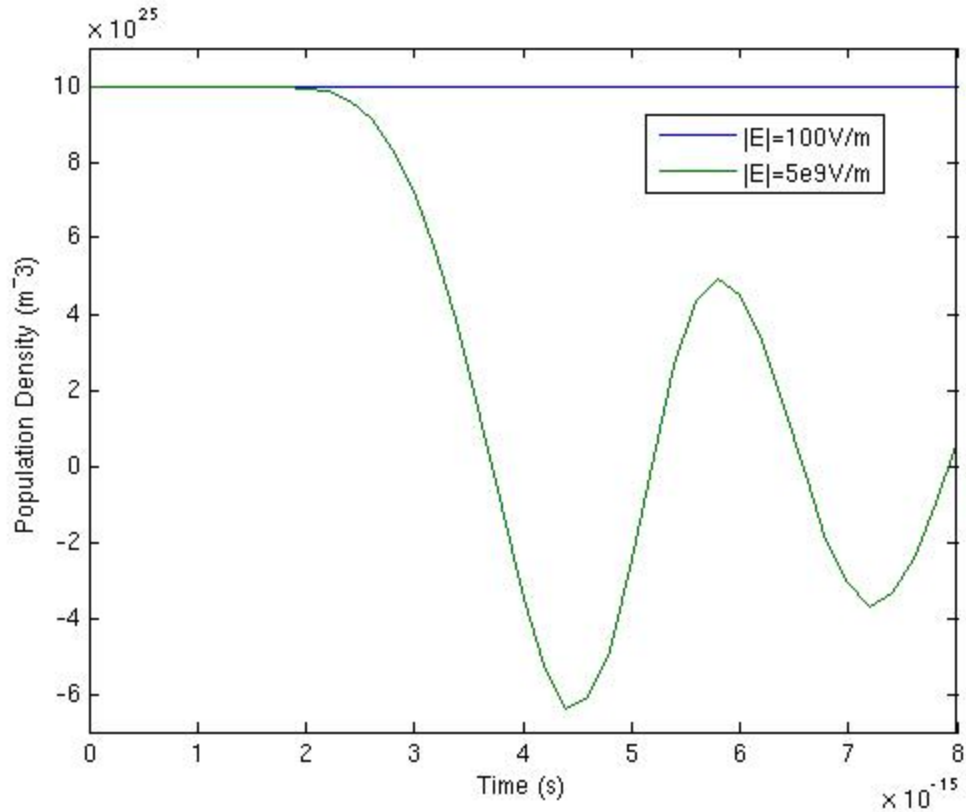


Figure 2 : The population density for the nonlinear simulation capability utilizing the polarization equation. This plot shows the linear (100 V/m) and nonlinear response (5e9 V/m).

Quench2d Extension Research

The Quench2d extension research generated results that impacted a number of Laboratory projects. Early work integrating EMSolve decay-diffusion work with the Quench2D beam propagation method yielded the capability to model the optical effects of x-ray irradiation in bulk semiconductor (which was used for preliminary simulation of the RadTracker project). The 3D extension of Quench2D was used to determine both forward and backward scattering of radiation induced carrier distributions.

During the project we were called upon to provide analysis for two Laboratory projects: RadSensor and RadTracker. Both of these projects used the change in refractive index of a semiconductor as a function of carrier density as a means of detecting radiation. We examined the scattering expected in a semiconductor Fabry-Perot interferometer for the RadSensor project as a function of scatterer index and location in the cavity. For the RadTracker project we coupled the 3D carrier decay-diffusion solver generated for EMSolve with the semiconductor bulk material model and a beam propagation simulator to determine the expected scattering as a function of time from the absorption of a pair of x-ray photons. Results of this simulation are shown in Figure 3.

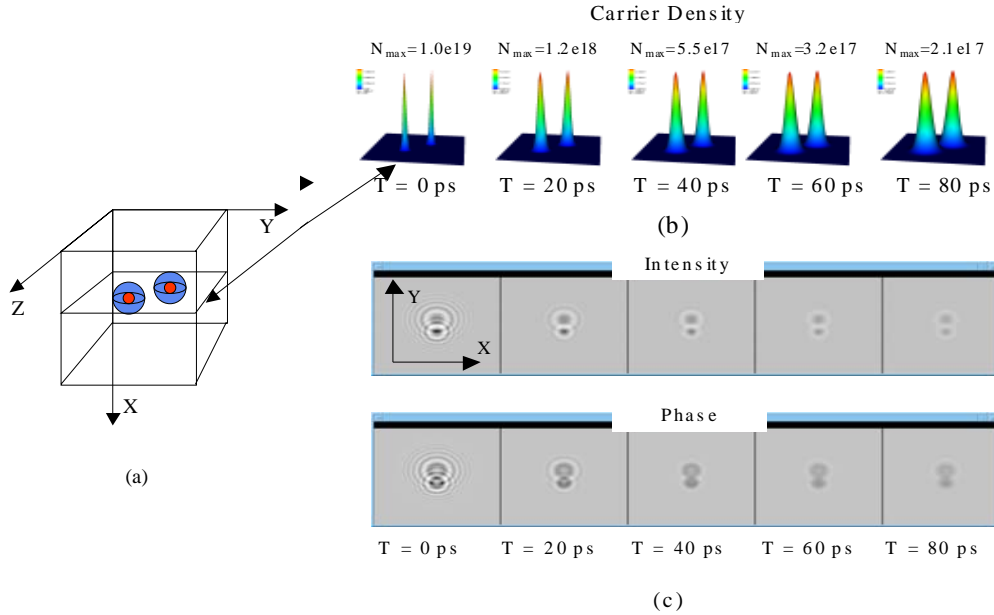


Figure 3. Coupling 3D carrier decay-diffusion simulation with a nonlinear bulk material model and a 3D optical beam propagation simulation (a) A cube of semiconductor, 10 microns on a side is hit by two x-rays. (b) The carrier density in the plane of the x-ray hits is shown as a function of time. The carrier density both diffuses and decays. (c) The perturbation in phase and intensity is shown as a function of time.

In addition to the work on the RadSensor and RadTracker projects our research work was

QED for Semiconductor Material Modeling Research

In the first year of this project a bulk semiconductor material model was built. In the subsequent years it was extended to model semiconductor quantum wells. These models were used to generate tables of material parameters that could be incorporated in the operations of the Quench3D and EMSolve codes. A full accounting of the results of this work has been written up in Appendix A.

Exit Plan

Many of the drivers that prompted the initiation of this work have evaporated over the life of the project. Major contributions that the project made included

- Simulation of gain lever based edge emitting laser logic. This was needed by the NSA WFO active-passive integration project. That project has ended successfully and papers have been written as a result [21,22].
- 1st and 2nd generation RadSensor modeling. This was needed for fast x-ray diagnostics on NIF. These projects are currently past the need for modeling.
- RadTracker modeling. The RadTracker project was discontinued.

In the meantime, new projects have arisen that are exploiting the new capabilities for designing:

- VCSEL based gas sensors for weapons program.
- Complex DFB EEL for Photonic-FPGA universal logic gates for DARPA (This work has already resulted in a patent disclosure and a paper [23] which is in review).
- Microring and microdisk resonators fabrication tolerance analysis for NSA WFO (which has resulted in a paper which is currently in review).

When the project began, Engineering had not yet become interested in THz technology. By virtue of being able to model both electrodynamics and carrier drift-diffusion we were able to simulate semiconductor photoconductivity and the Auston switch THz source/receiver. Our simulations were of great utility to the Engineering THz initiative, showing that multiple sources could be used to scale the power of the Auston switch [12].

The various components of this project also live on in a variety of applications. The vector extensions to the BPM method are being used for research on microring resonators [24] and fiber amplifiers. The virtual matrix work on EMSolve was incorporated into the PhD work of Aaron Fisher [16,25]. Work on VCSEL simulations is continuing and will eventually lead to the publication of a paper.

Summary

We now have a set of EM modeling tools that are capable of operating in the Laboratory's unique design space. We can model the effects of novel sources such as x-rays on semiconductor devices. We have extended the range of systems that can be simulated in full wave 3D by an order of magnitude. We have provided new code constructs that enable simple integration of new physics in computational EM modeling systems.

Acknowledgements

We wish to acknowledge the contributions of Aaron Fisher, Dan White, Jerry Burke, Kathleen Fasenfest, and Ellen Chang. In addition we acknowledge the efforts of Rob Sharpe in keeping this project focused and active.

References

1. D. M. Sullivan, "Nonlinear FDTD formulations using Z transforms," IEEE Trans. Microwave Theory Tech., vol. 43, pp. 676-682, Mar. 1995; D. M. Sullivan, "Z-transform theory and the FDTD method," IEEE Trans. Antennas Propagat., vol. 44, pp. 28-34, Jan. 1996; D. M. Sullivan, "A frequency-dependent FDTD method for biological applications," IEEE Trans. Microwave Theory Tech., vol. 40, pp. 532-539, Mar. 1992.
2. W. H. Weedon and C. M. Rappaport, "General method for FDTD modeling of wave propagation in arbitrary frequency-dispersive media," IEEE Trans. Antennas Propagat., vol. 45, pp. 401-410, Mar. 1997.

3. R. M. Joseph and A. Taflove, "FDTD Maxwell's equations models for nonlinear electrodynamics and optics," *IEEE Trans. Antennas Propagat.*, vol. 45, pp. 364-374, Mar. 1997; P. M. Goorjian, A. Taflove, R. M. Joseph, and S. C. Hagness, "Computational modeling of femtosecond optical solitons from Maxwell's equations," *IEEE J. Quantum Electron.*, vol. 28, no. 10, pp. 2416-2422, 1992; R. M. Joseph, P. M. Goorjian, and A. Taflove, "Direct time integration of Maxwell's equations in two-dimensional dielectric waveguides for propagation and scattering of femtosecond electromagnetic solitons," *Optics Lett.*, vol. 18, no. 7, pp. 491-493, 1993.
4. G. W. Zheng and K. S. Chen, "Transient analysis of dielectric step discontinuity of microstrip lines containing a nonlinear layer," *Int. J. Infrared Millim. Waves*, vol. 13, no. 8, pp. 1127-1137, 1992.
5. R. W. Ziolkowski and J. B. Judkins, "Applications of the nonlinear finite difference time domain (NL-FDTD) method to pulse propagation in nonlinear media: Self-focusing and linear-nonlinear interfaces," *Radio Sci.*, vol. 28, pp. 901-911, Sept.-Oct. 1993; R. W. Ziolkowski and J. B. Judkins, "Full-wave vector Maxwell equation modeling of the self-focusing of ultrashort optical pulses in a nonlinear Kerr medium exhibiting a finite response time," *J. Opt. Soc. Am., B Opt. Phys.*, vol. 10, pp. 186-198, Feb. 1993; R. W. Ziolkowski and J. B. Judkins, "Nonlinear finite-difference time-domain modeling of linear and nonlinear corrugated waveguides," *J. Opt. Soc. Am., B Opt. Phys.*, vol. 11, pp. 1565-1575, Sept. 1994; R. W. Ziolkowski, "The incorporation of microscopic material models into the FDTD approach for ultrafast optical pulse simulations," *IEEE Trans. Antennas Propagat.*, vol. 45, pp. 375-391, Mar. 1997.
6. P. Tran, "Optical switching with a nonlinear photonic crystal: A numerical study," *Optics Lett.*, vol. 21, pp. 1138-1140, Aug. 1996; P. Tran, "Optical limiting and switching of short pulses by use of a nonlinear photonic bandgap structure with a defect," *J. Opt. Soc. Am., B Opt. Phys.*, vol. 14, pp. 2589-2595, Oct. 1997; H-B. Lin et al., "Two-dimensional photonic Bandgap optical limiter in the visible", *Optics Lett.*, Vol. 23, No. 2, Jan. 1998, pp. 94-6; M. Bayindir et al., "Propagation of photons by hopping: A waveguiding mechanism through localized coupled cavities in three-dimensional photonic crystals", *Phys. Rev. B*, vol. 61, no.18, May 2001, pp. R11 855-58; E. Chow et al. "Quantitative analysis of bending efficiency in photonic-crystal waveguide bends at 1.55 μm wavelengths, *Opt. Lett.*, vol. 26, No. 5, March 1, 2001; Russell et al., "A neat idea [photonic crystal fibre]", *IEE Review*, vol.47, no.5, Sept. 2001, pp.19-23; Zhou WD et al., "Cylindrical microcavity light emitters realized with double-oxide-confinement or single-defect photonic bandgap crystals. [Conference Paper] 58th DRC. Device Research Conference. Conference Digest (Cat. No.00TH8526). IEEE. 2000, pp.115-16. Piscataway, NJ, USA.
7. Feit M.D. and Fleck J.A., "Wave-optics description of laboratory soft-x-ray lasers," *J. Opt. Soc. Am. B*, Vol. 7, No 10, pp. 2048-2060, October 1990; Lai J.W. and Lin C.F., "Carrier Diffusion Effect in Tapered Semiconductor-Laser Amplifier," *IEEE Journal of Quantum electronics*, Vol. 34, No. 7, pp. 1247-1256, July 1998.
8. Larry A. Coldren and Scott W. Corzine, *Diode Laser and Photonic Integrated Circuits*, Ed. Kai Chang, John Wiley & Sons, Inc., pp. 198-199; Fitz JL, Beard WT, Horst SC, Smith SD, "Integrated photonics inverter with gain," *IEEE Photonics*

- Technology Letters, Vol. 13, No. 5, pp. 478-80, 2001; Vawter GA, Blum O, Allerman A, Gao Y, Highly-efficient laser with self-aligned waveguide and current confinement by selective oxidation," 1999 LEOS Proceedings, Part Vol. 2, pp 531-2, 1999.
9. B. Demeulenaere et al., "Detailed Study of AlAs-Oxidized Apertures in VCSEL Cavities for Optimized Modal Performance", IEEE Journ. Quantum Electron., col. 35, no.3, March 1999, pp. 358-67; H. Rao et al., "VCSEL Design Using the Bidirectional Beam-Propagation Method", IEEE Journ. Quantum Electron., vol. 37, no.11, March 2001, pp 1435-40; M. Noble et al., "Analysis of Microcavity VCSEL Lasing Modes Using a Full-Vector Weighted Index Method", IEEE Journ. Quant. Electron., vol. 34, no. 10, Oct. 1998, pp. 1890-903. A. Vukovic et al., "Novel Hybrid Method for Efficient 3-D Fiber-to-Chip Coupling Analysis", IEEE Journ. Sel. Top. Quant. Electron., vol. 8, no. 6, Nov/Dec 2002, pp. 1285-92; J-P Hsu et al., "Methods for calculating the properties of polarization maintaining 3D waveguides in very thin multilayered structures", IEE Proc. Optoelectron., vol. 146, no. 3, June 1999, pp. 165-171; E. Montanari et al., "Finite-Element Full-Vectorial Propagation Analysis for Three-Dimensional-Varying Optical Waveguides", IEEE Journ Light. Technol., vol. 16, no.4, April 1998, pp. 703-14; P.V. Studenkov et al., "Monolithic Integration of an All-Optical Mach-Zehnder demultiplexer Using an Asymmetric Twin-Waveguide Structure", IEEE Photon. Technol. Lett., vol. 13, no. 6, June 2001, pp. 600-2
 10. Shultz D., Glingener C., Bludzuweit M., and Voges E., "Mixed Finite Element Beam Propagation Method," Journal of Lightwave Technology, Vol. 16, No. 7, pp. 1336-42, July 1998.
 11. Feng N-N., Zhou G-R., and Huang W-P., "An efficient Split-Step Time-Domain Beam-Propagation Method for Modeling of Optical Waveguide Devices," J. Lightwave Tech., Vol. 23, No. 6, pp. 2186-91, June 2005.
 12. J. M. Koning, "Terahertz Photo-Conductive Antenna Array Power Scaling Simulations," Proceedings IEEE APS, 2006, pp. 2631-2634.
 13. Smith P., Auston D., Nuss M., "Subpicosecond Photoconducting Dipole Antennas", IEEE J. Quantum Elect., v. 24, n. 2, pp. 255-260, 1980.
 14. Castillo P.; Koning J.; Rieben R.; White D., "A discrete differential forms framework for computational electromagnetics," Comp. Meth. Eng. Sci., Vol 5, No 4, pp 331-346, 2004.
 15. White D.A.; Koning J.; Rieben R.N.; Stowell M.; Fisher A.; Fasenfest B.; Rodrigue G.H., "EMSolve", {<http://www.llnl.gov/casc/emsolve>}.
 16. Fisher, A.; Rieben, R.N.; Rodrigue, G.H.; White, D.A., "A generalized mass lumping technique for vector finite-element solutions of the time-dependent Maxwell equations," IEEE Trans. Antennas and Propagation, vol.53, no.9, pp. 2900- 2910, Sept. 2005.
 17. S. H. Chang, A. Taflove, "Finite-difference time-domain model of lasing action in a four-level two-electron atomic model," Optics Express, Vol. 12, no. 16, 2004, pp.3827-3833.
 18. A. S. Nagra, R. A. York, "FDTD Analysis of Wave Propagation in Nonlinear Absorbing and Gain Media," IEEE Trans. On Ant. And Prop., Vol. 46, no. 3, 1998, pp. 334-340.

19. Y. Huang and S. T. Ho, "Computational model of solid-state, molecular, or atomic media for FDTD simulation based on multi-level multi-electron system governed by Pauli exclusion and Fermi-Dirac thermalization with application to semiconductor photonics," *Optics Express*, vol. 14, no. 8, 2006, pp.3569-3587.
20. A. E. Siegman, *Lasers*, Mills Valley CA, Univ. Science Books, 1986.
21. L. L. Goddard, J. S. Kallman, and T. C. Bond, "Rapidly reconfigurable all-optical universal logic gates," *invited paper*, Proc . SPIE 6368, OH-1-13, Oct. 2006.
22. M. D. Pocha, T. C. Bond, L. L. Goddard, R. J. Nikolic, S. P. Vernon, J. S. Kallman, E. M. Behymer, "Electrical and Optical Gain Lever Effects in InGaAs Double Quantum Well Diode Lasers," to be submitted to IEEE Journal of Quantum Electronics.
23. L. L. Goddard, T. C. Bond, J. S. Kallman, "An Architecture for Photonic Field Programmable Gate Arrays," to be submitted to CLEO 2007.
24. J. E. Heebner, T. C. Bond, J. S. Kallman, "Generalized Formulation for Bending and Edge Scattering Loss in Microdisk Resonators," to be submitted to Optics Letters.
25. A. Fisher, G. Rodrigue, D. White, "An Efficient Vector Finite Element Method for Nonlinear Electromagnetic Modeling," *Journal of Computational Physics* (in Review).

Appendix A: QED for Semiconductor Material Modeling Research
T. C. Bond and K. Fassenfest

A tool for modeling the dependence of gain and refractive index on wavelength and carrier density was developed for analyzing nonlinear effects in both heterostructure and quantum well (QW) semiconductor devices. Bandfilling, bandgap shrinkage, free carrier, and excitonic absorption effects were evaluated, and results were verified against those found in the literature. The model can be used in understanding the nonlinear characteristics of semiconductors under x-ray radiation, aiding in the design of sensitive high-speed radiation detection devices. Our objectives were to also create integrate modal dispersion effects into the modeling tool; and package it in a user-friendly environment.

Heterostructures

The main carrier related effects that induce changes of the absorption (gain) in bulk semiconductor material are bandgap shrinkage, bandfilling, free carrier absorption. Excitonic saturation exist but the excitonic feature is not very strong thus the effect s small. The refractive index change is related to absorption changes by the Kramers-Kronig integrals in the form

$$\Delta n(N, P, E) = \frac{\hbar c}{\pi} P \int_0^{\infty} \frac{\Delta \alpha(E') - \Delta \alpha(E)}{E'^2 - E^2} dE' + \frac{\hbar^2 c^2}{4E^2} \alpha(E) \Delta \alpha(E). \quad (1)$$

For finding absorption, parabolic bands were initially assumedⁱ. The optical absorption near the bandgap in a direct-band semiconductor was given as the square-root law:

$$\alpha_o(E) = \frac{C}{E} \sqrt{E - E_g} \quad E \geq E_g$$

$$\alpha_o(E) = 0 \quad E < E_g,$$

(2)

where $E = \hbar\omega$ is the photon energy, E_g is the bandgap energy, and C is a material constant.^{i,ii}

Bandgap Shrinkage Effect

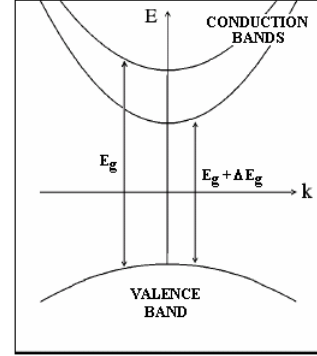
Injected electrons occupy states at the bottom of the conduction band, resulting in a lowering of the conduction band edge. The valence band edge similarly increases due to the presence of holes. The result is a shrinkage in the gap between the bands. The change in the bandgap is given by

$$\Delta E_g(\chi) = -\frac{\kappa}{\epsilon_s} \left(\frac{\chi}{\chi_{cr}} - 1 \right)^{1/3} \quad \chi \geq \chi_{cr}$$

$$\Delta E_g(\chi) = 0 \quad \chi < \chi_{cr}$$

(3)

where κ is a fitting parameter and χ_{cr} is the critical concentration of free carriers.



Bandfilling Effect

For bandfilling to occur in injected semiconductors, the density of states must be sufficiently low such that a small number of carriers can fill the bands. The effective bandgap increases, because electrons in the valence band require more energy to be excited into the conduction band. In the diagram, “1” marks the transition involving heavy holes, and “2” marks the transition involving light holes. Both are larger than the bandgap marked “ E_g .”

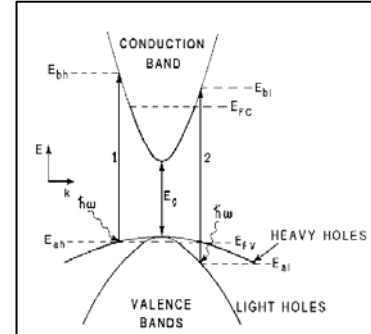
The formula given for change in absorption due to bandfilling must include bandgap shrinkage effects

$$\Delta \alpha(N, P, E) =$$

$$\frac{C_{hh}}{E} \sqrt{E - E_g - \Delta E_g} [f_v(E_{ah}) - f_c(E_{bh}) - 1]$$

$$+ \frac{C_{lh}}{E} \sqrt{E - E_g - \Delta E_g} [f_v(E_{al}) - f_c(E_{bl}) - 1]$$

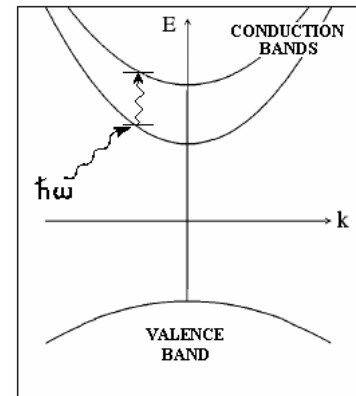
(4)



Free-Carrier Absorption

A free carrier can absorb a photon and move to a higher energy state within a band. This intraband absorption is sometimes called the “plasma effect.” The resulting index change may be calculated directly, rather than by Kramers-Kronig relations:

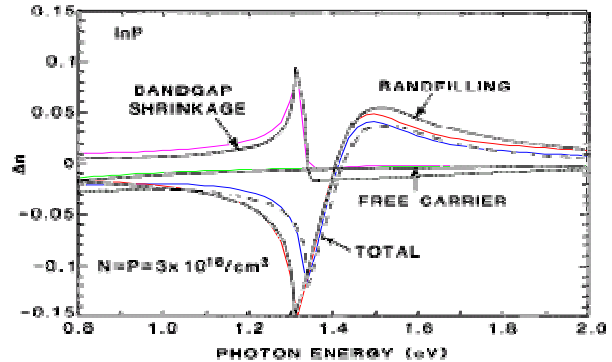
$$\Delta n = -\left(\frac{e^2 \lambda^2}{8\pi^2 c^2 \epsilon_o n} \right) \left\{ \frac{N}{m_e} + P \left(\frac{m_{hh}^{1/2} + m_{lh}^{1/2}}{m_{hh}^{3/2} + m_{lh}^{3/2}} \right) \right\}. \quad (5)$$



Validation

Below, our calculated change in refractive index is compared with Bennett's results. The material used was InP, with a carrier concentration of $3 \times 10^{18}/\text{cm}^3$.

The upper limit of integration on the Kramers-Kronig integral makes a significant impact on the results obtained. In addition, the inclusion of our added absorption term also has a significant effect on the results. For these reasons, the results shown above are believed to be in good agreement with those published by Bennett.

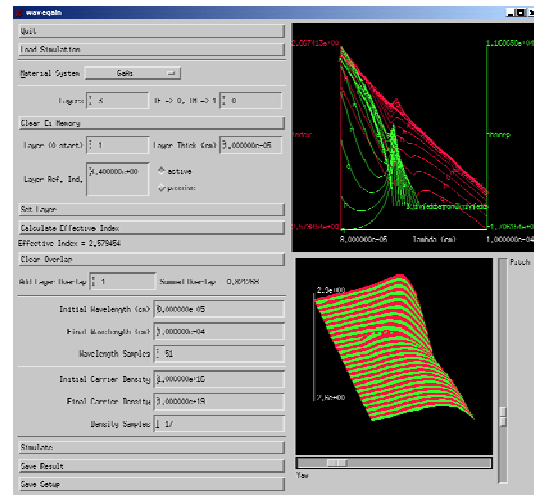


Integration with Mode Solver

The new modeling tool solves for the effective index inside a waveguiding structure.

Below is a screen shot of the new modeling tool “Wavegain.”

The upper graph shows both index and absorption vs. wavelength for a range of carrier concentrations. By clicking at a location on the 2D graph, the user may select a particular photon wavelength at which to view the refractive index vs. carrier concentration. Alternatively, the user may click and drag, moving the mouse rightwards, over a region of the graph to zoom in on a particular range of wavelengths. To return to the original plot, the user simply clicks and drags while moving the mouse to the left. The lower graph shows index (height) versus carrier concentration and wavelength (lateral dimensions).



The Quench3D code can read the output of the modeling tool as a lookup table, which will aid the analysis of spatial and transient radiation effects on semiconductors.

Eventually, the simple model of base absorption (Eq. 1) was replaced by a more sophisticated model based on Adachi's workⁱⁱⁱ. The real and imaginary parts of the relative permittivity are computed due to each material energetic transition, and the total permittivity is found by summing the permittivities of all the transitions. The calculations of the E_1 , $E_1+\Delta_1$, E_0' , E_g^{ID} , and E_{0ex} transition permittivities were done according to the model from Adachi's book. The E_0 and $E_0+\Delta_0$ transition permittivities were calculated by splitting the light hole, heavy hole, and split-off transitions into separate components of the total permittivity. The saturation of the excitonic peak was computed using a formulation similar to the Kawase model^{iv}.

The sum of the permittivities is given by

$$\varepsilon(E) = \varepsilon_0(E) + \varepsilon_0 d_0(E) + \varepsilon_1(E) + \varepsilon_1 d_1(E) + \varepsilon_2(E) + \varepsilon_1 D(E) + \varepsilon_0 \text{ex}(E) \quad (6)$$

where the real part of the permittivity $\varepsilon_1(E) = \text{Re}(\varepsilon(E))$ and the imaginary part of the permittivity $\varepsilon_2(E) = \text{Im}(\varepsilon(E))$. The base refractive index n and extinction coefficient κ can then be solved for as

$$n(E) = \sqrt{\frac{\sqrt{(\varepsilon_1(E))^2 + (\varepsilon_2(E))^2} + \varepsilon_1(E)}{2}} \quad (7)$$

$$\kappa(E) = \sqrt{\frac{\sqrt{(\varepsilon_1(E))^2 + (\varepsilon_2(E))^2} - \varepsilon_1(E)}{2}} \quad (8)$$

From the extinction coefficient, we can find the absorption $\alpha_0(E) = \frac{4\pi E \kappa(E)}{c \hbar}$, where c is

the speed of light and \hbar is Planck constant. The effect of the exciton saturation on the

absorption was calculated as $\alpha_{ex,sat}(E, N) = \frac{\alpha_{ex,unsat}(E)}{1 + \frac{N}{N_s}}$ and its change as

$$\Delta\alpha_{ex}(E, N) = \alpha_{ex,sat}(E, N) - \alpha_{ex,unsat}(E).$$

Quantum Wells

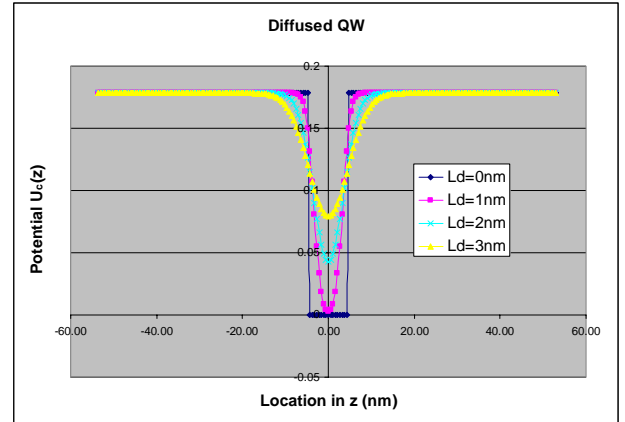
Devices often use quantum wells (QWs) to maximize the changes in absorption. A QW consist of a region with smaller bandgap embedded between two barriers, regions with larger bandgap.

Diffusion and Band Structure

The structure modeled is an unstrained, undoped single quantum well. The carriers are assumed to be injected into the quantum well from the ends of the barrier region. Intermixing effects are included for modeling the properties of actual devices. For an annealing time t and a diffusion coefficient D , the diffusion length L_d is defined as $L_d = (Dt)^{1/2}$. For $\text{Al}_w\text{Ga}_{1-w}\text{As}$ — GaAs , the fraction w of Al across the QW structure is given as

$$w(z) = w_0 \left\{ 1 - \frac{1}{2} \left[\text{erf} \left(\frac{L_z + 2z}{4L_d} \right) + \text{erf} \left(\frac{L_z - 2z}{4L_d} \right) \right] \right\} \quad (9)$$

where w_0 is the as-grown Al fraction in the barrier, L_z is the width of the QW, z is the growth axis, and erf is the error function. Note that AlGaAs is the barrier material and GaAs is the well material. The center of the QW is located at $z = 0^v$. Depending on the diffusion length the band structure of the QW (between two barriers) smoothens as shown in the following picture



In a QW, the energy levels are quantized, with values of E_{rl} , where $l = 1, 2, \dots$ are the allowed energy levels. The probability a particle r is at energy E_{rl} at location z is given by $|\Psi_{rl}(z)|^2$. To find $\Psi_{rl}(z)$ and E_{rl} , the Schrödinger-like equation.

$$-\frac{\hbar^2}{2} \left[\frac{1}{m_r^*(z)} \frac{d\Psi_{rl}(z)}{dz} \right] + U_r(z) \Psi_{rl}(z) = E_{rl} \Psi_{rl}(z) \quad (10)$$

is solved using a one-dimensional finite difference method the central difference form is used to second-order accuracy, adequate for the piecewise linear potential function and effective mass chosen here. The central difference form is used to second-order accuracy, adequate for the piecewise linear potential function and effective mass chosen here. The eigenvectors $\Psi_{rl}(z)$ must be normalized so that the probability of finding a particle in the QW structure is equal to 1, which is equivalent to $\frac{1}{\sqrt{L_{QW}}} \int \Psi_{rl}(z) dz = 1$, where L_{QW} is the width of the QW.

Self-consistent energy levels

The presence of charged particles in the QW structure modifies the potential profile. To find the variation in the potential profile due to the presence of these particles, first the carrier spatial distributions must be found.

$$\left. \begin{array}{l} n_e(z) \\ p_{hh}(z) \\ p_{lh}(z) \end{array} \right\} = \sum_{l=1}^P |\Psi_{rl}(z)|^2 g_r(E_{rl}) f(E_{rl}, E_{F,r}), \quad (11)$$

where $f(E, E_F)$ is the Fermi function (probability that an energy state is filled) and g_r is the density of states (number of electronic states at an energy level) $n_e(z)$ is the carrier distribution of electrons in the conduction band, $p_{hh}(z)$ is the carrier distribution of heavy holes in the valence band, and $p_{lh}(z)$ is the carrier distribution of light holes in the valence band. The total number of carriers in the conduction band is $N_0 = \frac{1}{L_{QW}} \int_{-z_B}^{+z_B} n_e(z) dz$,

and the total number of carriers in the valence band is $P_0 = \frac{1}{L_{QW}} \int_{-z_B}^{+z_B} (p_{hh}(z) + p_{lh}(z)) dz$.

After the spatial carrier distributions $n_e(z)$, $p_{hh}(z)$, and $p_{lh}(z)$ are known, the many-body carrier effects are estimated from Poisson's equation

$$\frac{d^2}{dz^2} V_e(z) = \frac{e^2}{\epsilon_r \epsilon_0} (p_{hh}(z) + p_{lh}(z) - n_e(z)), \quad (12)$$

Similar to the Schrödinger-like equation, Poisson's equation is solved by finite difference method using. The potential function for carriers is then given as the sum of the initial potential profile and the many-body correction term $V_r(z)$. Using this new potential profile, the Schrödinger-like equation and Poisson's equation are solved iteratively until all eigenvalues E_{rl} are consistent between iterations to 1 meV.

Permittivity

The imaginary part of the permittivity is found as the sum of the contributions from interband, intraband, and continuum transitions. The interband transitions occur between valence band states and conduction band states. The interband contribution to the imaginary permittivity is^{vi}

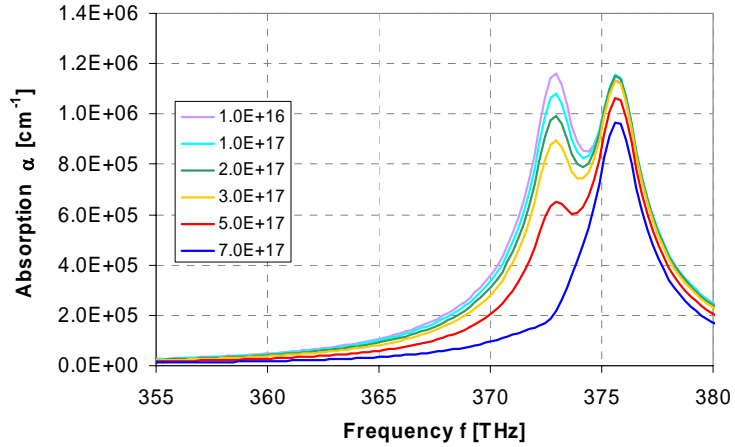
$$\varepsilon_{r,\text{interband}}''(\omega) = 4 \left(\frac{m_r}{\hbar^2 L_{QW}} \right) \left(\frac{8}{\pi} \right) \sum_{c=1}^{N_c} \sum_{r=hh, lh} \sum_{v=1}^{N_v} \left[\left| \langle \Psi_c | \Psi_{rv} \rangle \right|^2 \left(\frac{\hbar^2}{6m_e (E_{c,v} + E_b)^2} \right) \left(\frac{E_g (E_g + \Delta)}{E_g + \frac{2}{3} \Delta} \right) \times \right. \\ \left. \left(f_v(\hbar\omega, E_{F,v}) - f_c(\hbar\omega, E_{F,c}) \right) \left(\frac{\Gamma}{(E_{c,v} + E_b - \hbar\omega)^2 + \Gamma^2} \right) P^{TE, TM} \right], \quad (13)$$

where $E_{c,v} = E_g + E_{cl} + E_{vl}$ is the bandgap energy including shrinkage effects and E_b is the binding energy of the exciton. The term $f_v - f_c$ takes into account the band filling effects. The polarization coefficient $p^{TE, TM}$ is given by

$$p^{TE} = \begin{cases} \frac{3}{4}(1 + E_R), & hh \\ \frac{1}{4}(5 - 3E_R), & lh \end{cases} \quad p^{TM} = \begin{cases} 0, & hh \\ \frac{1}{2}(1 + 3E_R), & lh \end{cases}, \quad E_R = \frac{E_{cl} + E_{vl'}}{E_{cl} + E_{vl'} + \hbar\omega}. \quad (14)$$

Results

An example of the implementation of the described model shown in the accompanying picture, where the absorption vs. frequency for a TE polarized light is derived for a 7nm GaAs QW with 40nm Al_{0.2}Ga_{0.8}As barriers and a diffusion length of 2nm.



ⁱ B. R. Bennett, R. A. Soref, and J. A. del Alamo, *IEEE J. Quantum Elect.*, vol. 26, pp. 113-122, 1990.

ⁱⁱ J. P. Weber, *IEEE J. Quantum Elect.*, vol. 30, pp. 1801-1816, 1994.

ⁱⁱⁱ Adachi S., *J. Appl. Phys.* **53**(12), Dec 1982, p. 8775-8792; *Physical Review B*, vol. 35, no. 14, 15 May 1987, p. 7454-7463; *Physical Review B*, vol. 39, no. 17, 15 June 1989, p. 12612-12621.; *J. Appl. Phys.* **66**(12), 15 Dec 1989, p. 6030-6040; *Physical Properties of III-V Semiconductor Compounds: InP, InAs, GaAs, GaP, InGaAs, and InGaAsP*. New York: John Wiley & Sons, 1992.

^{iv} Kawase M et al., *IEEE Journal of Quantum Electronics*, vol 30, no. 4, April 1994, p. 981-988.

^v K.S. Chan et al., *Optoelectronic Properties of Semiconductors and Superlattices*, vol. 8. Australia: Gordon and Breach Science Publishers, 2000.

^{vi} Chuang, S-L et al., *Physical Review B*, vol. 43, no. 2, p. 1500-1509

Appendix B: Coupled Drift-Diffusion Electrodynamics Photonics Simulation Code in *EMSolve*

1 Introduction

The Auston switch [1] combines a semiconductor device with an ultrafast optical pulse to create Terahertz radiation. A simulation of this device will need to solve the electrodynamic wave equation for the optical pulse and Terahertz radiation as well as a carrier dynamics equation for the semiconducting material. A simple flow chart showing the interaction between the carrier dynamics/transport module and the electrodynamics solver is showing Figure 1. It is important to note that thermal effects play a large part in both the carrier transport and electrodynamics portions of this flowchart. Within the constraint of the total simulation time thermal effects will not play a large role and are therefore neglected.

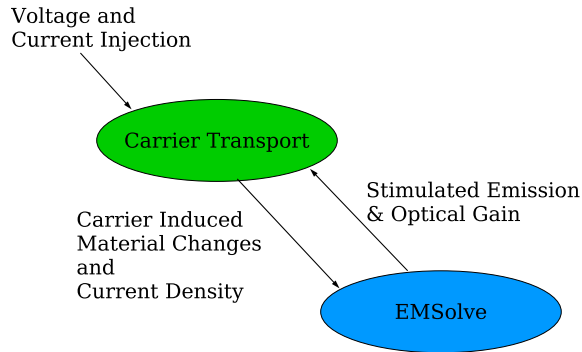


Figure 1: Flow chart for electrodynamic carrier dynamics interaction.

2 Maxwell's Equations

In electromagnetics we have the three-dimensional vector electric and magnetic fields E , H , the three-dimensional vector electric and magnetic flux densities D , B , and the constitutive relations

$$D = \bar{\epsilon}E, B = \bar{\mu}H. \quad (1)$$

Here we write Maxwell's Equations in terms of E and B ,

$$\bar{\epsilon} \frac{\partial}{\partial t} E = \nabla \times \frac{1}{\bar{\mu}} B - \bar{\sigma} E - J_s, \quad (2)$$

$$\frac{\partial}{\partial t} B = -\nabla \times E, \quad (3)$$

$$\nabla \cdot \bar{\epsilon} E = \rho, \quad (4)$$

$$\nabla \cdot B = 0, \quad (5)$$

$$E \times \hat{n} = E_{bc} \text{ on } \Gamma_D, \quad (6)$$

$$E(t=0) = E_{ic}, \quad B(t=0) = B_{ic}. \quad (7)$$

where Γ_D is the part of the boundary of the region Ω where Dirichlet boundary conditions are applied. Note that J_s is an independent current source term, which may or may not exist for every problem. The material properties $\bar{\epsilon}, \bar{\mu}, \bar{\sigma}$ are in general real symmetric positive definite tensors that are inhomogeneous in space and time dependent. Equations (2)-(5) can be solved by *EMSolve*. Alternatively, these equations can be combined to yield an second-order wave equation for E alone,

$$\bar{\epsilon} \frac{\partial^2}{\partial t^2} E + \bar{\sigma} \frac{\partial}{\partial t} E = -\nabla \times \frac{1}{\bar{\mu}^{-1}} \nabla \times E - \frac{\partial}{\partial t} J_s, \quad (8)$$

$$E \times \hat{n} = E_{bc} \text{ on } \Gamma_D, \quad (9)$$

$$E(t=0) = E_{ic}, \quad \frac{\partial}{\partial t} E(t=0) = \frac{\partial}{\partial t} E_{ic}. \quad (10)$$

which can also be solved by *EMSolve*. When solving (8) it is a simple matter to also compute the magnetic field by integrating (3). At present, our solution to (2)-(5) is explicit, with a time step restriction $\Delta t = O\left(\frac{\Delta h}{c}\right)$, where c is the speed of light in the medium of interest, and Δh is the smallest element dimension in the mesh. In *EMSolve* we can solve (8) implicitly using a Newmark-Beta type method, which is unconditionally stable. This does not mean that we can take arbitrarily large time steps, in practice it is still necessary to resolve the electromagnetic waves in order for the wave equation to provide reasonable solutions. However, there are applications, such as quasi-statics or diffusion, where the time scale is such that it is not necessary or desirable to resolve the wave motion.

3 Carrier Dynamics

The semiconductor region in the simulation domain will not have static material properties if any charge carriers have been created within the material. The equations that describe the dynamics of the semiconductor material carriers in an electric field are the drift-diffusion equations.

The drift diffusion equations derive from the charge density continuity equation (11).

$$-\frac{\partial}{\partial t}\rho = \nabla \cdot J \quad (11)$$

This equation can be split into two equations, one containing the electron charge density $\rho_n = -qn$ and the other containing the hole number density $\rho_p = qp$ where $\rho = q(p - n + N_d - N_A)$. The values q, n and p are the absolute value of the electric charge $|e|$, the electron number density and the hole number density respectively. The total current density is split into the current density contributions from the electrons and the holes (12).

$$J = J_n + J_p \quad (12)$$

The resulting equations are shown in (13)

$$-(-q)\left(\frac{\partial}{\partial t}n + R - G\right) = \nabla \cdot J_n \quad (13)$$

$$-(+q)\left(\frac{\partial}{\partial t}p + R - G\right) = \nabla \cdot J_p \quad (14)$$

where R and G are the recombination and generation rates and

$$J_n = qn\mu_n E + qD_n \nabla n \quad (15)$$

$$J_p = qp\mu_p E - qD_p \nabla p. \quad (16)$$

The values μ_n, μ_p, D_n and D_p are the electron and hole mobilities and the electron and hole diffusivities respectively.

Using the relation for the conductivity tensor σ (17),

$$\sigma = q(\mu_n n + \mu_p p) \quad (17)$$

the total current density can be written as in (18).

$$J = \sigma E + q(D_n \nabla n - D_p \nabla p) \quad (18)$$

The equations for the electron and hole number densities are shown in (19).

$$\frac{\partial}{\partial t}n = \nabla \cdot n\mu_n E + \nabla \cdot D_n \nabla n - q(R - G) \quad (19)$$

$$\frac{\partial}{\partial t}p = -\nabla \cdot p\mu_p E + \nabla \cdot D_p \nabla p + q(R - G) \quad (20)$$

4 Simulation Domains

The simulation domain consists of a $150 \times 150 \times 400$ micrometer box. The first $O=20-40$ micrometers in the z -dimension are an air region. An antenna with thickness $P=2$ micrometers in the z -dimension is defined by a region removed from the mesh. The remainder of the domain $Q=380-360$ micrometers is a semiconductor material. A two-dimensional representation is shown in Figure 2. The value for L is 105 micrometers, F is 10 micrometers, H is set at 35,55 or 85 micrometers and G is 150 micrometers.

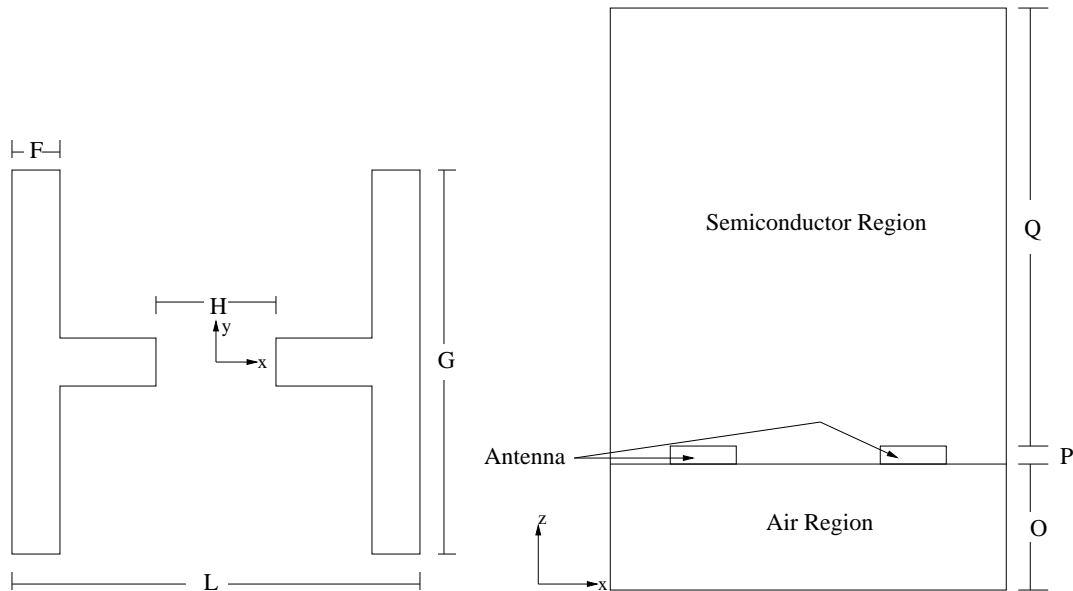


Figure 2: Two dimensional antenna design.

5 Finite Element Discretization

5.1 FEMSTER

FEMSTER is a class library of higher-order discrete differential forms that is used within the *EMSolve* code [2]. If you are familiar with concepts from differential forms (tangent vectors, wedge product, exterior derivative, hodge-star operator, etc.) that's great, FEMSTER provides discrete versions of these concepts. In standard finite element language, FEMSTER contains all the data structures and operations required to compute local finite element matrices: elements (tetrahedrons, hexahedrons, prisms), basis functions (or shape functions), quadrature rules, linear forms, and bilinear forms. FEMSTER provides the gradient, curl, and divergence operators, as well as the, div-grad, curl-curl, and grad-div operators. Note that arbitrary partial derivative operators are not included, as these do not fit nicely into the framework of differential forms, and fortunately

are not needed for computational electromagnetics. The basis function class hierarchy contains four forms of basis functions, simply called 0-forms, 1-forms, 2-forms, and 3-forms. Derived from each of these classes are sub-classes for the element types tetrahedron, hexahedron, and prism, and derived from each of these types is a further specialization for the degrees-of-freedom, i.e. interpolatory, spectral, hierarchical, etc. The critical step in using FEMSTER is to decide what form should be used for each physical quantity. The essential properties of the forms are:

0-forms are continuous scalar basis functions that have a well-defined gradient. These basis functions are a finite subspace of $\mathcal{H}(grad)$. These basis functions are suitable for the electric potential ϕ , temperature T , etc. The basis functions are dimensionless, hence the degrees-of-freedom have the same units as the field being approximated. If the field is temperature, the degrees-of-freedom have units of temperature. The gradient of a 0-form basis function can be represented, exactly, as a combination of 1-form basis functions, i.e. $dW^0 \in W^1$.

1-forms are vector basis functions with continuous tangential components across elements, but discontinuous normal components. They have a well defined curl, but do not have a well defined gradient or divergence. These basis functions are a finite subspace of $\mathcal{H}(curl)$. The basis functions have units of m^{-1} . For example the electric field has units of *Volts/m* and the degrees-of-freedom will therefore have units of *Volts*. It is a simple matter to integrate 1-forms along the edges of a mesh, but surface integrals are not well defined. These basis functions are ideally suited for the electric field E , the magnetic field H , the magnetic vector potential A , etc. The curl of a 1-form basis function can be represented, exactly, as a combination of 2-form basis functions, i.e. $dW^1 \in W^2$. The null space of the curl operator on 1-forms is, exactly, the space of gradients of 0-forms, $dW^1 = 0$ implies $W^1 = dW^0$, for simply-connected regions.

2-forms are vector basis functions with continuous normal components across elements, but discontinuous tangential components. They have a well defined divergence, but do not have a well defined gradient or curl. These basis functions are a finite subspace of $\mathcal{H}(div)$. The basis functions have units of m^{-2} . For example the electric current density has units of *Amperes/m²*, therefore the degrees-of-freedom have units of *Amperes*. It is a simple matter to integrate 2-forms over surfaces of a mesh, but line integrals are not well defined. These basis functions are ideally suited for the electric flux density D , the magnetic flux density B , etc. The divergence of a 2-form basis function can be represented, exactly, as a combination of 3-form basis functions. The null space of the divergence operator on 2-forms is, exactly, the space of curls of 1-forms.

3-forms are discontinuous scalar basis functions. They can't be differentiated. They can be integrated over a volume, but not over a surface or a line. These basis functions are a finite subspace of L_2 . The basis functions have units of m^{-3} . For example, charge density has units of *Coulombs/m³* and the degrees-of-freedom will therefore have units of *Coulombs*. These basis functions are ideally suited for the electric charge density ρ , the energy density ϵ , etc.

FEMSTER computes the following “mass”, “stiffness”, and “derivative” matrices, where the

superscript 0,1,2,3 denotes the degree of the form,

$$\mathbf{M}_0(\alpha)_{ij} = \int_{\Omega} \alpha W_i^0 W_j^0 d\Omega \quad (21)$$

$$\mathbf{M}_1(\alpha)_{ij} = \int_{\Omega} \alpha W_i^1 \cdot W_j^1 d\Omega \quad (22)$$

$$\mathbf{M}_2(\alpha)_{ij} = \int_{\Omega} \alpha W_i^2 \cdot W_j^2 d\Omega \quad (23)$$

$$\mathbf{M}_3(\alpha)_{ij} = \int_{\Omega} \alpha W_i^3 W_j^3 d\Omega \quad (24)$$

$$\mathbf{S}_0(\alpha)_{ij} = \int_{\Omega} \alpha \nabla W_i^0 \cdot \nabla W_j^0 d\Omega \quad (25)$$

$$\mathbf{S}_1(\alpha)_{ij} = \int_{\Omega} \alpha \nabla \times W_i^1 \cdot \nabla \times W_j^1 d\Omega \quad (26)$$

$$\mathbf{S}_2(\alpha)_{ij} = \int_{\Omega} \alpha \nabla \cdot W_i^2 \nabla \cdot W_j^2 d\Omega \quad (27)$$

$$\mathbf{D}_{01}(\alpha)_{ij} = \int_{\Omega} \alpha \nabla W_i^0 \cdot W_j^1 d\Omega \quad (28)$$

$$\mathbf{D}_{12}(\alpha)_{ij} = \int_{\Omega} \alpha \nabla \times W_i^1 \cdot W_j^2 d\Omega \quad (29)$$

$$\mathbf{D}_{23}(\alpha)_{ij} = \int_{\Omega} \alpha \nabla \cdot W_i^2 W_j^3 d\Omega \quad (30)$$

The “mass” matrices \mathbf{M} and the “stiffness” matrices \mathbf{S} are square and map p -forms to p -forms, the “derivative” matrices \mathbf{D} are rectangular and map p -forms to $(p+1)$ -forms. It can be shown that

$$\mathbf{D}_{01} = \mathbf{M}_1 \mathbf{K}_{01} \quad (31)$$

$$\mathbf{S}_0 = (\mathbf{K}_{01})^T \mathbf{M}_1 \mathbf{K}_{01} \quad (32)$$

$$\mathbf{D}_{12} = \mathbf{M}_2 \mathbf{K}_{12} \quad (33)$$

$$\mathbf{S}_1 = (\mathbf{K}_{12})^T \mathbf{M}_2 \mathbf{K}_{12} \quad (34)$$

$$\mathbf{D}_{23} = \mathbf{M}_3 \mathbf{K}_{23} \quad (35)$$

$$\mathbf{S}_2 = (\mathbf{K}_{23})^T \mathbf{M}_3 \mathbf{K}_{23} \quad (36)$$

where $\mathbf{K}_{p(p+1)}$ is a “topological derivative” matrix. This matrix is the discretization of the exterior derivative operator d from differential geometry, $dW^p = W^{(p+1)}$. This matrix depends upon the mesh connectivity, but is independent of the nodal coordinates. It does not involve an integral over the element, and it does not involve any material properties. While seemingly abstract, it is enormously valuable in practice. The FEMSTER library computes the topological derivative matrices \mathbf{K}_{01} , \mathbf{K}_{12} , and \mathbf{K}_{23} . Given a p -form quantity X with basis function expansion

$$X = \sum_{i=1}^n x_i W_i^p, \quad (37)$$

and a $(p + 1)$ -form quantity Y with basis function expansion

$$Y = \sum_{i=1}^n y_i W_i^{(p+1)}, \quad (38)$$

the exterior derivative (gradient, curl, divergence for $p = 0$, $p = 1$, and $p = 2$, respectively) is given by

$$\mathbf{y} = \mathbf{K}_{p(p+1)} \mathbf{x}. \quad (39)$$

It can be shown that

$$\mathbf{K}_{12} \mathbf{K}_{01} = 0 \quad (40)$$

$$\mathbf{K}_{23} \mathbf{K}_{12} = 0 \quad (41)$$

which are the discrete versions of the identities $\nabla \times \nabla F = 0$ and $\nabla \cdot \nabla \times F = 0$, respectively. These identities are satisfied in the discrete sense, exactly (well, to machine precision), for any mesh and any order basis function.

FEMSTER contains some additional miscellaneous functionality. In some circumstances it is necessary to convert a p -form to a $(3 - p)$ -form, i.e. a Hodge-star operation. A classic example is converting a "cell-center" quantity to a "nodal" quantity. In our finite element setting the Galerkin procedure prescribes rectangular matrices of the form

$$(\mathbf{H}_{p(3-p)})_{ij} = \int_{\Omega} W_i^p \wedge W_j^{(3-p)} d\Omega \quad (42)$$

which produces optimal (in the least-square error sense) Hodge-star operators for arbitrary order basis functions. FEMSTER also computes a variety of "load vectors" that are used as source terms in finite element discretizations,

$$\mathbf{f}_{0j} = \int_{\Omega} f W_j^0 d\Omega \quad (43)$$

$$\mathbf{f}_{1j} = \int_{\Omega} f \cdot W_j^1 d\Omega \quad (44)$$

$$\mathbf{f}_{2j} = \int_{\Omega} f \cdot W_j^2 d\Omega \quad (45)$$

$$\mathbf{f}_{3j} = \int_{\Omega} f \cdot W_j^3 d\Omega \quad (46)$$

$$\mathbf{g}_{0j} = \int_{\Gamma} g W_j^0 d\Gamma \quad (47)$$

$$\mathbf{g}_{1j} = \int_{\Gamma} g \cdot W_j^1 d\Gamma \quad (48)$$

$$\mathbf{g}_{2j} = \int_{\Gamma} g \cdot W_j^2 d\Gamma \quad (49)$$

5.2 FEM Discretization of the Wave Equation

For the electric field and current density equations we will discretize them in terms of the 1-form edge basis functions $W_i^1 \in H(\text{curl})$.

$$E = \sum_{i=1}^{N_{edges}} e_i W_i^1 \quad (50)$$

$$J = \sum_{i=1}^{N_{edges}} j_i W_i^1 \quad (51)$$

The variational form of the second order electric field wave equation (8) becomes (52).

$$\begin{aligned} & \frac{\partial^2}{\partial t^2} (\bar{\epsilon} E, E^*) + \frac{\partial}{\partial t} (\bar{\sigma}_E E, E^*) = \\ & -(\bar{\mu}^{-1} \nabla \times E, \nabla \times E^*) - \frac{\partial}{\partial t} (J_s, E^*) - \oint_{\Gamma} \bar{\mu}^{-1} (E^* \times \nabla \times E) \cdot \hat{n} \nabla E^* \in \mathcal{H}(\text{curl}) \end{aligned} \quad (52)$$

In this equation the notation (E, E^*) represents an integral over the problem domain Ω and Γ represents the boundary of Ω .

Entering the expansions for the electric field and electric and magnetic current densities results in the second order electric wave equation (53).

$$\mathbf{M}_1(\bar{\epsilon}) \frac{\partial^2}{\partial t^2} e + \mathbf{M}_1(\bar{\sigma}_E) \frac{\partial}{\partial t} e = -\mathbf{S}_1(\bar{\mu}^{-1}) e - \mathbf{M}_1 \frac{\partial}{\partial t} j - \oint_{\Gamma} (\bar{\mu}^{-1} W_j^1 \times \nabla \times E) \cdot \hat{n} \quad (53)$$

The essential and natural boundary conditions can be determined from the boundary condition term in the variational equation (52). In this wave equation the essential boundary condition corresponds to the Dirichlet boundary condition and the natural boundary condition corresponds to the Neumann boundary condition (54)

$$\begin{aligned} E \times \hat{n} &= D \text{ on } \Gamma_D \\ \nabla \times E \times \hat{n} &= N \text{ on } \Gamma_N \end{aligned} \quad (54)$$

where Γ_D and Γ_N represent the portion of the domain boundary on which Dirichlet and Neumann boundary conditions are applied, respectively. The boundary term can be evaluated in terms of the discrete basis functions and is shown in (55). The resulting matrix is zero due to the choice of test space.

$$\oint_{\Gamma} \bar{\mu}^{-1} (E^* \times \nabla \times E) \cdot \hat{n} = (\bar{\mu}^{-1} \nabla \times W_i^1, W_j^1 \times \hat{n})_{\Gamma} = 0, W_j^1 \in \mathcal{H}(\text{curl}) \quad (55)$$

5.2.1 NewmarkBeta Discretization

The NewmarkBeta integrator, used by the Maxwell_TwoStepInt application, solves equation (53) while treating the stiffness and conductivity matrices implicitly. The conductivity matrix multiplies the first derivative of the E field. This time derivative is approximated using a difference scheme

centered at time $m * dt$ rather than the usual $(m - \frac{1}{2}) * dt$. The stiffness matrix multiplies a weighted average of the E field values at all three available time steps. The parameter β determines these weights. With these discretization schemes the equation becomes:

$$M_1(\bar{\epsilon}) \frac{e^{m+1} - 2e^m + e^{m-1}}{dt^2} = -S_1(\bar{\mu}^{-1})(\beta e^{m+1} + (1 - 2\beta)e^m + \beta e^{m-1}) - M_1 \left. \frac{\partial j}{\partial t} \right|^m - M_1(\bar{\sigma}) \frac{e^{m+1} - e^{m-1}}{2dt} \quad (56)$$

Moving terms involving the unknown, e^{m+1} , to the left hand side leads to:

$$\begin{aligned} & \left(M_1(\bar{\epsilon}) + \beta dt^2 S_1(\bar{\mu}^{-1}) + \frac{dt}{2} M_1(\bar{\sigma}) \right) e^{m+1} = \\ & (2M_1(\bar{\epsilon}) - (1 - 2\beta) dt^2 S_1(\bar{\mu}^{-1})) e^m + \\ & \left(-M_1(\bar{\epsilon}) - \beta dt^2 S_1(\bar{\mu}^{-1}) + \frac{dt}{2} M_1(\bar{\sigma}) \right) e^{m-1} - \\ & dt^2 M_1 \left. \frac{\partial j}{\partial t} \right|^m \end{aligned}$$

6 Implementation of NewmarkBeta

In this method the E field at the next time step is solved for directly so the voltage boundary condition must impose the actual voltage as its constraint.

Again, the current source is applied using a ‘load vector’ to save a matrix-vector multiplication as well as saving the memory necessary to store an additional 1-form mass matrix. Also, note that in equation (56) the first derivative of the current appears so the function used to define the current source must be the first derivative of the intended current density.

Table 1: Voltage and Current Sources in NewmarkBeta

Source	Method	Derivative
Voltage	Dirichlet BC	0 th
Electric Current	RHS Load Vector	1 st
Magnetic Current	N/A	–

This method employs as many as six matrices: the solver matrix, 1-form mass matrix using $\bar{\epsilon}$, 1-form mass matrix using $\bar{\sigma}$, 1-form stiffness matrix using $\bar{\mu}^{-1}$, 1-form ABC matrix, and a topological derivative matrix (if the B field is being updated.) It also uses three 1-form vectors internally. These are in addition to the three vectors that can be passed as arguments to the `update()` method.

Table 2: Linear System Overview for NewmarkBeta

Form Type	Number of			
	Matrices	Vectors	Mat-Vecs	Solves
1-Form	5	3	4	1
2-Form	0	0	0	0
12-Form	1	-	1	-

6.1 FEM Discretization of the Carrier Equations

In this section the finite-element discretizations for the advection diffusion equations presented in (19) are derived. The finite-element method chosen is a two-step Taylor-Galerkin finite-element method [3]. This method is chosen due to the inability of the standard Rayleigh-Ritz-Galerkin method to handle the advection terms.

The Taylor-Galerkin method uses a Taylor expansion to second order in time for the number density advection-diffusion equation and a standard Galerkin spatial discretization. The method begins with the conservative form of the advection equation (57).

$$\frac{\partial}{\partial t} n + \nabla \cdot F = 0 \quad (57)$$

where $F \equiv -\mu_n n E$. The equation (57) is then Taylor-expanded to second order in time (58).

$$n^{m+1} = n^m + \Delta t \frac{\partial}{\partial t} n^m + \frac{\Delta t^2}{2} \frac{\partial^2}{\partial t^2} n^m + O(\Delta t^3) \quad (58)$$

Substituting (57) into (58) gives (59).

$$n^{m+1} = n^m - \Delta t \nabla \cdot F^m - \frac{\Delta t^2}{2} \nabla \cdot \left[\frac{\partial}{\partial t} F^m \right] \quad (59)$$

The two-step Taylor-Galerkin method obtains the flux derivatives at time m by first evaluating an equation for the density at time $m + \frac{1}{2}$ (60).

$$n^{m+\frac{1}{2}} = n^m - \frac{\Delta t}{2} \nabla \cdot F^m \quad (60)$$

This is the first step of the algorithm. These values are then used to determine the flux equation for time $m + \frac{1}{2}$ which is shown in (61)

$$F^{m+\frac{1}{2}} = F^m + \frac{\Delta t}{2} \frac{\partial}{\partial t} F^m \quad (61)$$

where the time derivative is (62).

$$\frac{\partial}{\partial t} F^m = \frac{2}{\Delta t} \{ F^{m+\frac{1}{2}} - F^m \} \quad (62)$$

Substituting (62) into (59) gives (63)

$$n^{m+1} = n^m - \Delta t \nabla \cdot F^{m+\frac{1}{2}} \quad (63)$$

which is the second step of the Taylor-Galerkin algorithm.

The two variables n (64) and F (65) are expanded in 0-form, nodal, basis functions and 1-form, edge, basis functions respectively.

$$n = \sum_{i=1}^{N_{nodes}} \alpha_i N_i \quad (64)$$

$$F = \sum_{l=1}^{N_{edges}} f_l W_l \quad (65)$$

The two equations (60) and (63) corresponding to the two parts of the Taylor-Galerkin algorithm are discretized and presented in (66) and (67). In the second step equation (67) the half step flux is constructed from the half-step numerical density $f^{m+\frac{1}{2}} \equiv -\mu_n n^{m+\frac{1}{2}} e^m$

$$\alpha^{m+\frac{1}{2}} = \alpha^m + \frac{\Delta t}{2} M_0^{-1} D_{01}^T f^m \quad (66)$$

$$\alpha^{m+1} = \alpha^m + \Delta t M_0^{-1} D_{01}^T f^{m+\frac{1}{2}} \quad (67)$$

In order to solve the equation (67) iteratively, some papers use a lumped 0-form mass matrix, M_{0L} , to provide a low order approximation which acts like a diffusive term. There are also low-order, high-order methods and upwinding, limiting issues that I am looking into.

The dispersion term is added to the right hand side of equation (67) giving (68).

$$\alpha^{m+1} = \alpha^m + \Delta t M_0^{-1} [D_{01}^T f^{m+\frac{1}{2}} - S_0(D_n) \alpha^m] \quad (68)$$

The mobilities μ_n, μ_p as well as the diffusion coefficients are functions of the electric field E . An equation relating the electron mobility with the electric field is shown in (69).

$$\mu_n(E) = \left\{ \frac{\mu_{n0} + \left(\frac{v_{sat}}{E_{th}}\right) \left(\frac{|E|}{E_{th}}\right)^3}{1 + \left(\frac{|E|}{E_{th}}\right)^4} \right\} \quad (69)$$

where μ_{n0} , v_{sat} and E_{th} are the electron low field mobility, saturation velocity and the threshold field magnitude respectively. Even though the hole mobilities are smaller the velocity still reaches a large value and will need to be dealt with as well. For GaAs the saturation velocity is $1e7 \frac{cm}{s}$.

6.2 Coupling the Carrier Equations with the Electric Field Wave Equation

The coupling between the two equations comes through the current density J . The value for J as shown in the (18) involves the conductivity tensor σ as well as a current density due to the diffusive terms. The drift diffusion equation requires the total electric field supplied by the solution of the wave equation and Poisson's equation. Because the source term for the density equations (19) involve the divergence of the electric field as well as the total electric field, it remains to be seen if the electric field from the wave equation and poisson equation need to be integrated together.

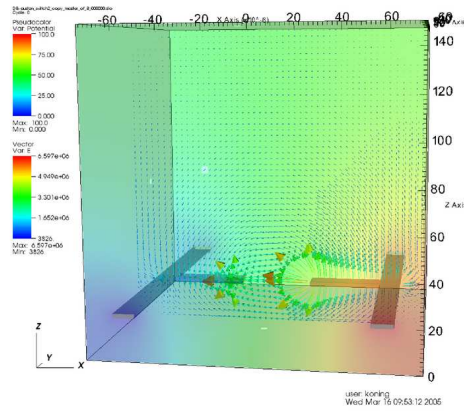
7 Results for Initial Electric Field and Potential Simulations

In this section the geometries listed above are used to determine the initial condition for the Auston switch system. In each case 100 V is applied across the antenna. This can be seen in the plots below by the blue (0V) and red (100V) colors over the antenna region. A plane has been sliced out of the domain to display the electric field vector plot for each geometry. In the three plots the distance between the antenna “fingers” has been varied with all other parameters remaining constant.

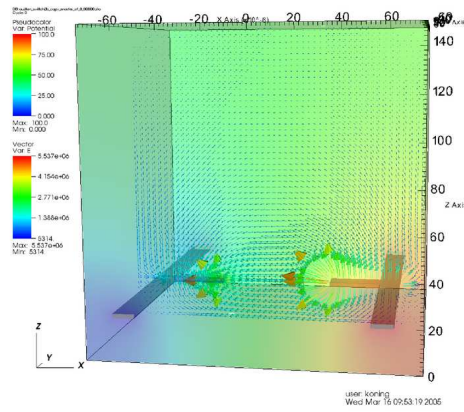
The three plots show the electric field strength is decreasing into the gap with larger gap length.

8 Results for Initial Auston Switch Simulations with Gaussian Time Pulse

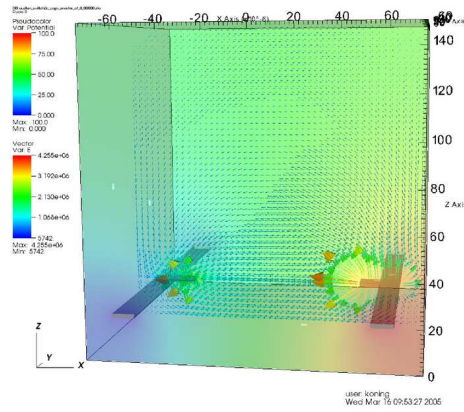
An initial Auston switch was simulated using a current source with constant magnitude in the x-direction and a Gaussian time pulse with FWHM=0.3 picoseconds. The geometry for this simulation is shown in Figure 4. The field at 0.8 picoseconds is shown in Figure 5.



$H=35 \mu\text{m}.$



$H=55 \mu\text{m}.$



$H=85 \mu\text{m}.$

Figure 3: Initial electric field and potential for varying geometries.

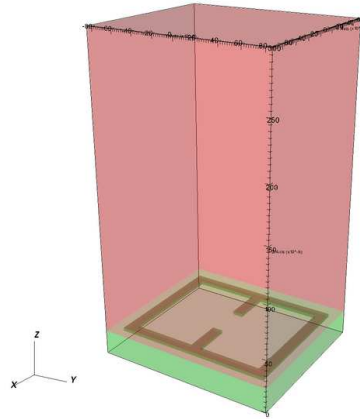


Figure 4: Geometry for Auston switch with Gaussian current source.

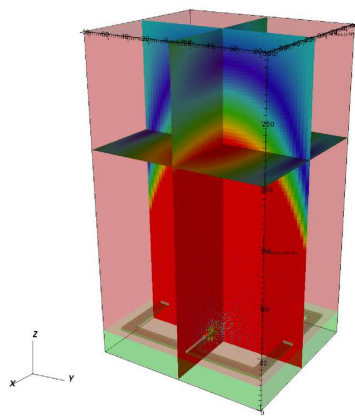


Figure 5: Electric Field magnitude and vector plot for $t=0.8$ picoseconds.

9 Results for One Dimensional Simulations

Using the values for GaAs as the active material a one-dimensional simulation for the drift-diffusion equation is used to determine the time scales for the Auston switch. The matlab script used for these simulations is listed in the Appendix. Currently only the electron, hole diffusion is implemented. The simulation is run on the drift time scale which is $1.5467 \times 10^{-13}s$ while the diffusion time scale is $6.6294 \times 10^{-12}s$. In figure Figure 6 plots are shown for charge density, potential, electron and hole densities as well as total current density for 1000 timesteps with a timestep of $1.16 \times 10^{-13}s$. The final timestep is shown in Figure 7.

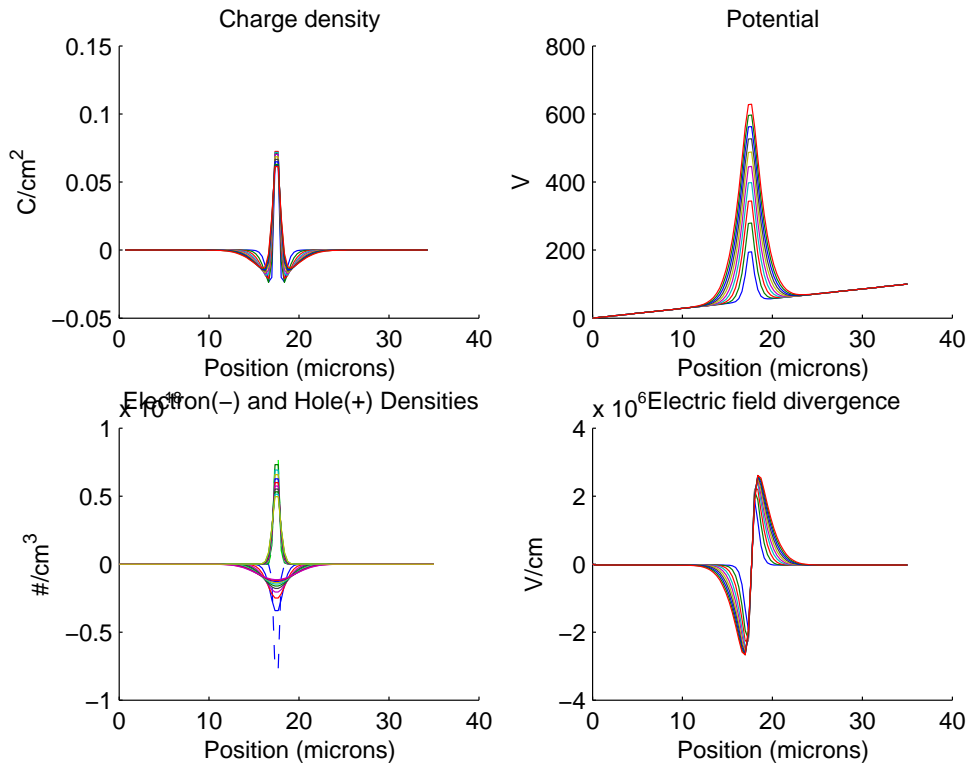


Figure 6: Carrier dynamics diffusion results with snapshot interval 100.

In figure Figure 8 the snapshots for a simulation for a fixed electric field are shown. The carrier motion is not fed back into the Poisson equation for electric field evolution. The potential for the resulting charge distribution is displayed separately showing the large discontinuity. It is apparent in the figure that the hole drift time is much much longer than the electron drift time.

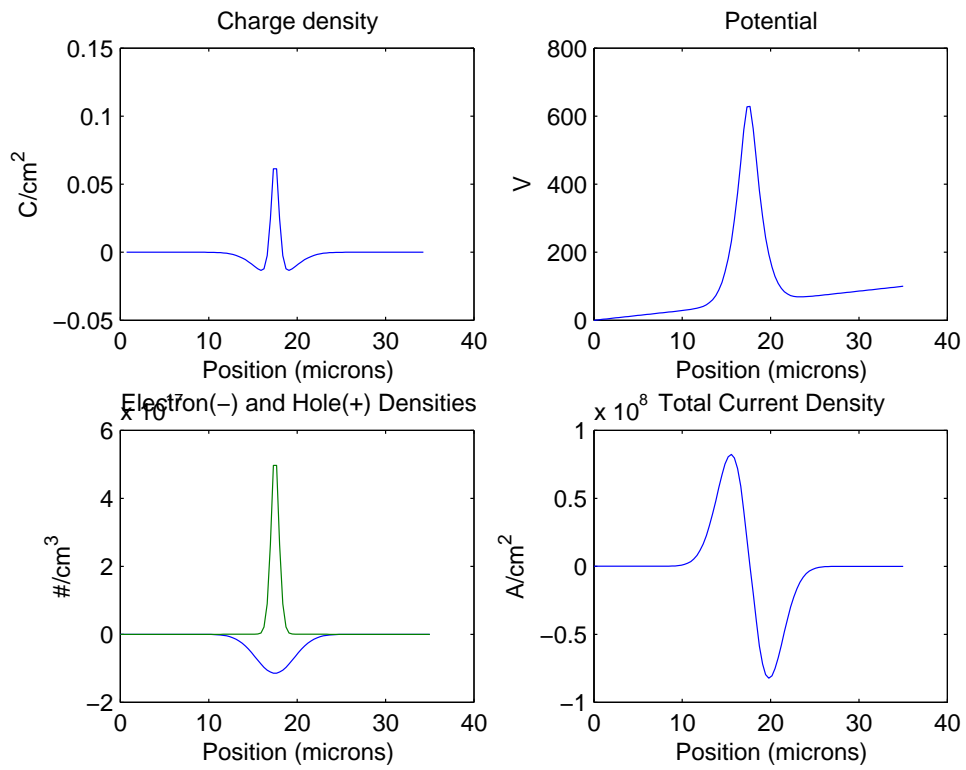


Figure 7: Carrier dynamics diffusion final results.

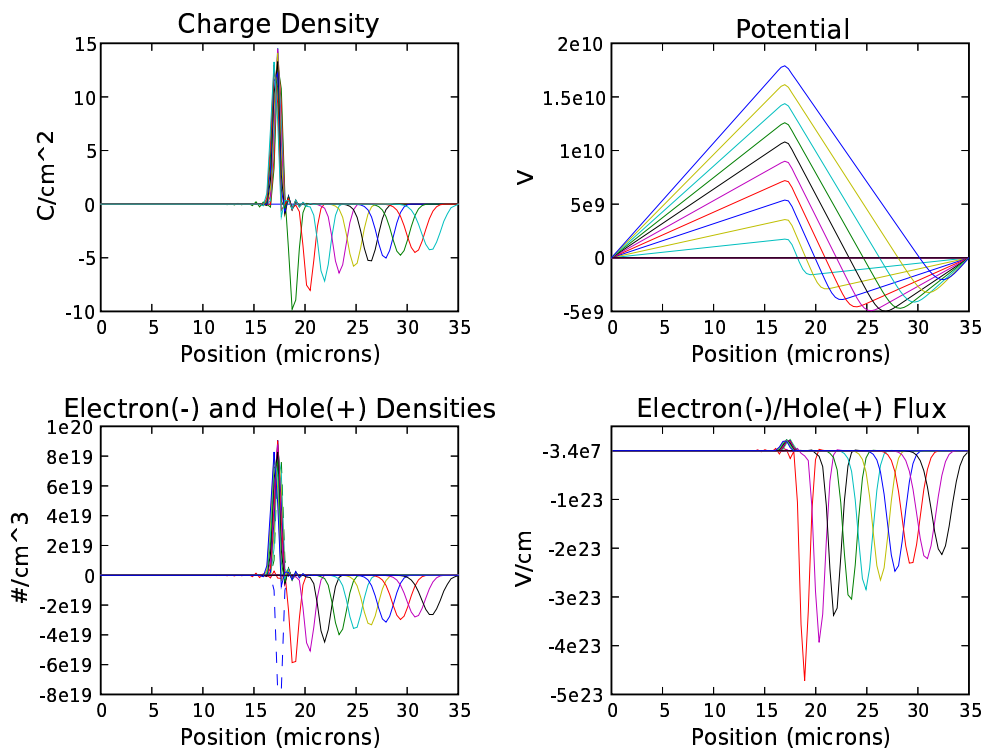


Figure 8: Carrier dynamics drift diffusion with fixed Electric field.

10 Conclusions

The coupled Drift-Diffusion Electrodynamics simulation capability described in here is targeted at semiconductor photonic devices with requirements for precision in all three dimensions. The full Maxwell and Drift-Diffusion equations implemented with the finite element method allow arbitrary order basis functions and arbitrary geometries. While the size of the simulation domain is limited due to computational expense of the finite element method, the parallel nature of the simulation code allows for realistic simulation domains.

References

- [1] P. R. Smith, D. H. Auston, and M. C. Nuss, “Subpicosecond photoconducting dipole antennas,” *IEEE J. Quantum Elect.*, vol. 24, no. 2, pp. 255–260, 1988.
- [2] P. Castillo, J. Koning, R. Rieben, M. Stowell, and D. White, “Discrete differential forms: A novel methodology for robust computational electromagnetics,” Tech. Rep. UCRL-ID-151522, Lawrence Livermore National Laboratory, Center for Applied Scientific Computing, January 2003.
- [3] J. A. Peraire, O. C. Zienkiewicz, and K. Morgan, “Shallow water problems: a general explicit formulation,” *Internat. J. Numer. Methods Engrg.*, vol. 22, pp. 547–574, 1986.

Appendix C: Nonlinear Absorbing and Gain Media in *EMSolve*

1 Introduction

Nonlinear gain and absorption in lasing media have been analysed using the finite difference time-domain (FDTD) method using an auxiliary differential equation (ADE) [1], [2]. In this paper the application of the ADE concept to a finite element discretization is developed. The finite element method used in this paper is the discrete differential forms finite element method implemented in the *EMSolve* code. This code uses the finite element library FEMSTER to implement grad, curl and divergence conforming arbitrary order basis functions. The nonlinear material models are implemented using both a Lorentzian model for the gain and a more advanced two-electron four-level model using the Pauli Exclusion principle. These equations incorporate rate equations that model the dynamics of the lasing media's atomic populations.

2 Maxwell's Equations

In electromagnetics we have the three-dimensional vector electric and magnetic fields \mathbf{E} , \mathbf{H} , the three-dimensional vector electric and magnetic flux densities \mathbf{D} , \mathbf{B} , macroscopic polarization \mathbf{P} , current density \mathbf{J} and the constitutive relations

$$\mathbf{D} = \bar{\epsilon}\mathbf{E}, \mathbf{B} = \bar{\mu}\mathbf{H}. \quad (1)$$

In this version of the nonlinear dynamics solver, the second order wave equation is solved (2).

$$\bar{\epsilon} \frac{\partial^2}{\partial t^2} \mathbf{E} + \bar{\sigma} \frac{\partial}{\partial t} \mathbf{E} = -\nabla \times \frac{1}{\bar{\mu}^{-1}} \nabla \times \mathbf{E} - \frac{\partial}{\partial t} \mathbf{J}_s - \frac{\partial^2}{\partial t^2} \mathbf{P}, \quad (2)$$

$$\frac{\partial}{\partial t} \mathbf{B} = -\nabla \times \mathbf{E}, \quad (3)$$

$$\nabla \cdot \mathbf{B} = 0, \quad (4)$$

$$\mathbf{E} \times \hat{n} = \mathbf{E}_{bc} \text{ on } \Gamma_D, \quad (5)$$

$$\mathbf{E}(t=0) = \mathbf{E}_{ic}, \quad \frac{\partial}{\partial t} \mathbf{E}(t=0) = \frac{\partial}{\partial t} \mathbf{E}_{ic}. \quad (6)$$

where Γ_D is the part of the boundary of the region Ω where Dirichlet boundary conditions are applied. Note that \mathbf{J}_s is an independent current source term, which may or may not exist for every problem. The material properties $\bar{\epsilon}, \bar{\mu}, \bar{\sigma}$ are in general real symmetric positive definite tensors that are inhomogeneous in space and time dependent.

The second order wave equation with polarization term is implemented in the code *EMSolve*. When solving (2) it is a simple matter to also compute the magnetic field by integrating (3). At present, our solution to (2)-(6) is explicit, with a time step restriction $\Delta t = O\left(\frac{\Delta h}{c}\right)$, where c is the speed of light in the medium of interest, and Δh is the smallest element dimension in the mesh. In *EMSolve* we can solve (2) implicitly using a Newmark-Beta type method, which is unconditionally stable. This does not mean that we can take arbitrarily large time steps, in practice it is still necessary to resolve the electromagnetic waves in order for the wave equation to provide reasonable solutions.

3 Polarization Dynamics

The region in the simulation with nonlinear materials will be modeled by the two-electron, two or four level polarization equation implemented through an auxiliary differential equation as derived in [1]. Each of the electrons is modeled as a dipole. For each dipole \mathbf{P}_i is the polarization, \mathbf{E} is the electric field and N_i correspond to the electron population densities. The variables γ_i and ω_i correspond to the damping constant through radiation loss, the resonant frequencies and. The values for ζ_i are $\zeta_a = \frac{6\pi\epsilon_0}{\omega_{21}^2\tau_{21}}$ and $\zeta_b = \frac{6\pi\epsilon_0}{\omega_{30}^2\tau_{30}}$. The total polarization from both dipoles is including in the polarization term in Maxwell's equations $\frac{d^2}{dt^2} \mathbf{P} = N_{density} \frac{d^2}{dt^2} (\mathbf{P}_a + \mathbf{P}_b)$.

$$\begin{aligned} \frac{d^2}{dt^2} \mathbf{P}_a + \gamma_a \frac{d}{dt} \mathbf{P}_a + \omega_a^2 \mathbf{P}_a &= \zeta_a (N_2 - N_1) \mathbf{E} \\ \frac{d^2}{dt^2} \mathbf{P}_b + \gamma_b \frac{d}{dt} \mathbf{P}_b + \omega_b^2 \mathbf{P}_b &= \zeta_b (N_3 - N_0) \mathbf{E} \end{aligned} \quad (7)$$

The population density probability equations for the four levels including the loss of efficiency due to the Pauli exclusion principle are shown in (8). The electron population density probabilities \tilde{N}_i in each level i are related to the pumping $\mathbf{E} \cdot \frac{d}{dt} \mathbf{P}_i$ and emission $\frac{(N_i - N_j)}{\tau_{ij}}$. The levels are separated by an energy $\hbar\omega_i$ for each dipole. The value τ_{ij} defines the decay time from level i to level j .

$$\begin{aligned}
\frac{d}{dt}\tilde{N}_3 &= -\frac{\tilde{N}_3(1-\tilde{N}_2)}{\tau_{32}} - \frac{\tilde{N}_3(1-\tilde{N}_0)}{\tau_{30}} + \frac{1}{\hbar\omega_b}\mathbf{E}\cdot\frac{d}{dt}\mathbf{P}_b \\
\frac{d}{dt}\tilde{N}_2 &= \frac{\tilde{N}_3(1-\tilde{N}_1)}{\tau_{32}} - \frac{\tilde{N}_2(1-\tilde{N}_0)}{\tau_{21}} + \frac{1}{\hbar\omega_a}\mathbf{E}\cdot\frac{d}{dt}\mathbf{P}_a \\
\frac{d}{dt}\tilde{N}_1 &= \frac{\tilde{N}_2(1-\tilde{N}_2)}{\tau_{21}} - \frac{\tilde{N}_1(1-\tilde{N}_2)}{\tau_{10}} - \frac{1}{\hbar\omega_a}\mathbf{E}\cdot\frac{d}{dt}\mathbf{P}_a \\
\frac{d}{dt}\tilde{N}_0 &= \frac{\tilde{N}_3(1-\tilde{N}_0)}{\tau_{30}} + \frac{\tilde{N}_1(1-\tilde{N}_0)}{\tau_{10}} - \frac{1}{\hbar\omega_b}\mathbf{E}\cdot\frac{d}{dt}\mathbf{P}_b
\end{aligned} \tag{8}$$

An alternative method for the auxiliary polarization equation was also implemented. This method discussed in [2] does not include the Pauli exclusion principle. The polarization equation derived from the electron oscillator or Lorenz model for this method is shown in (9).

$$\frac{d^2}{dt^2}\mathbf{P}_N + \gamma_N\frac{d}{dt}\mathbf{P}_N + \omega_a^2\mathbf{P}_N = \zeta\Delta N\mathbf{E} \tag{9}$$

In this case the decay constant is given by $\gamma_N = \gamma_r + \gamma_{nr} + \frac{2}{T_2}$ which is the actual linewidth of the transition. Here γ_r is the radiative energy decay rate, γ_{nr} is the non-radiative energy decay rate and T_2 describes the mean time between dephasing events. The value ζ is defined as $\zeta = \frac{6\pi\epsilon_0}{\omega_a^2\tau_{21}}$. As in the previous model this model depends on the dynamic difference between the energy levels $\Delta N(t) = N_1(t) - N_2(t)$. The values N_i are defined as the population density.

The population density equations in his case are given by (10).

$$\begin{aligned}
\frac{d}{dt}N_3 &= W_p - \frac{N_3}{\tau_3} \\
\frac{d}{dt}N_2 &= \frac{N_3}{\tau_{32}} - \frac{N_2}{\tau_2} + \frac{1}{\hbar\omega_a}\mathbf{E}\cdot\frac{d}{dt}\mathbf{P} \\
\frac{d}{dt}N_1 &= \frac{N_3}{\tau_{31}} + \frac{N_2}{\tau_{21}} - \frac{N_1}{\tau_1} - \frac{1}{\hbar\omega_a}\mathbf{E}\cdot\frac{d}{dt}\mathbf{P}
\end{aligned} \tag{10}$$

The values for τ_{ij} are as above, but this model has a constant total inverse transition probability per unit time to all lower energy levels given by τ_i . External pumping of the media is introduced through the variable W_p .

4 Finite Element Discretization

4.1 FEMSTER

FEMSTER is a class library of higher-order discrete differential forms that is used within the *EMSolve* code [3]. If you are familiar with concepts from differential forms (tangent vectors, wedge product, exterior derivative, hodge-star operator, etc.) that's great, FEMSTER provides

discrete versions of these concepts. In standard finite element language, FEMSTER contains all the data structures and operations required to compute local finite element matrices: elements (tetrahedrons, hexahedrons, prisms), basis functions (or shape functions), quadrature rules, linear forms, and bilinear forms. FEMSTER provides the gradient, curl, and divergence operators, as well as the, div-grad, curl-curl, and grad-div operators. Note that arbitrary partial derivative operators are not included, as these do not fit nicely into the framework of differential forms, and fortunately are not needed for computational electromagnetics. The basis function class hierarchy contains four forms of basis functions, simply called 0-forms, 1-forms, 2-forms, and 3-forms. Derived from each of these classes are sub-classes for the element types tetrahedron, hexahedron, and prism, and derived from each of these types is a further specialization for the degrees-of-freedom, i.e. interpolatory, spectral, hierarchical, etc. The critical step in using FEMSTER is to decide what form should be used for each physical quantity. The essential properties of the forms are:

0-forms are continuous scalar basis functions that have a well-defined gradient. These basis functions are a finite subspace of $\mathcal{H}(grad)$. These basis functions are suitable for the electric potential ϕ , temperature T , etc. The basis functions are dimensionless, hence the degrees-of-freedom have the same units as the field being approximated. If the field is temperature, the degrees-of-freedom have units of temperature. The gradient of a 0-form basis function can be represented, exactly, as a combination of 1-form basis functions, i.e. $dW^0 \in W^1$.

1-forms are vector basis functions with continuous tangential components across elements, but discontinuous normal components. They have a well defined curl, but do not have a well defined gradient or divergence. These basis functions are a finite subspace of $\mathcal{H}(curl)$. The basis functions have units of m^{-1} . For example the electric field has units of *Volts/m* and the degrees-of-freedom will therefore have units of *Volts*. It is a simple matter to integrate 1-forms along the edges of a mesh, but surface integrals are not well defined. These basis functions are ideally suited for the electric field E , the magnetic field H , the magnetic vector potential A , etc. The curl of a 1-form basis function can be represented, exactly, as a combination of 2-form basis functions, i.e. $dW^1 \in W^2$. The null space of the curl operator on 1-forms is, exactly, the space of gradients of 0-forms, $dW^1 = 0$ implies $W^1 = dW^0$, for simply-connected regions.

2-forms are vector basis functions with continuous normal components across elements, but discontinuous tangential components. They have a well defined divergence, but do not have a well defined gradient or curl. These basis functions are a finite subspace of $\mathcal{H}(div)$. The basis functions have units of m^{-2} . For example the electric current density has units of *Amperes/m²*, therefore the degrees-of-freedom have units of *Amperes*. It is a simple matter to integrate 2-forms over surfaces of a mesh, but line integrals are not well defined. These basis functions are ideally suited for the electric flux density D , the magnetic flux density B , etc. The divergence of a 2-form basis function can be represented, exactly, as a combination of 3-form basis functions. The null space of the divergence operator on 2-forms is, exactly, the space of curls of 1-forms.

3-forms are discontinuous scalar basis functions. They can't be differentiated. They can be integrated over a volume, but not over a surface or a line. These basis functions are a finite subspace of L_2 . The basis functions have units of m^{-3} . For example, charge density has units of *Coulombs/m³* and the degrees-of-freedom will therefore have units of *Coulombs*. These basis functions are ideally suited for the electric charge density ρ , the energy density ϵ , etc.

FEMSTER computes the following “mass”, “stiffness”, and “derivative” matrices, where the superscript 0,1,2,3 denotes the degree of the form,

$$\mathbf{M}_0(\alpha)_{ij} = \int_{\Omega} \alpha W_i^0 W_j^0 d\Omega \quad (11)$$

$$\mathbf{M}_1(\alpha)_{ij} = \int_{\Omega} \alpha W_i^1 \cdot W_j^1 d\Omega \quad (12)$$

$$\mathbf{M}_2(\alpha)_{ij} = \int_{\Omega} \alpha W_i^2 \cdot W_j^2 d\Omega \quad (13)$$

$$\mathbf{M}_3(\alpha)_{ij} = \int_{\Omega} \alpha W_i^3 W_j^3 d\Omega \quad (14)$$

$$\mathbf{S}_0(\alpha)_{ij} = \int_{\Omega} \alpha \nabla W_i^0 \cdot \nabla W_j^0 d\Omega \quad (15)$$

$$\mathbf{S}_1(\alpha)_{ij} = \int_{\Omega} \alpha \nabla \times W_i^1 \cdot \nabla \times W_j^1 d\Omega \quad (16)$$

$$\mathbf{S}_2(\alpha)_{ij} = \int_{\Omega} \alpha \nabla \cdot W_i^2 \nabla \cdot W_j^2 d\Omega \quad (17)$$

$$\mathbf{D}_{01}(\alpha)_{ij} = \int_{\Omega} \alpha \nabla W_i^0 \cdot W_j^1 d\Omega \quad (18)$$

$$\mathbf{D}_{12}(\alpha)_{ij} = \int_{\Omega} \alpha \nabla \times W_i^1 \cdot W_j^2 d\Omega \quad (19)$$

$$\mathbf{D}_{23}(\alpha)_{ij} = \int_{\Omega} \alpha \nabla \cdot W_i^2 W_j^3 d\Omega \quad (20)$$

The “mass” matrices \mathbf{M} and the “stiffness” matrices \mathbf{S} are square and map p -forms to p -forms, the “derivative” matrices \mathbf{D} are rectangular and map p -forms to $(p+1)$ -forms. It can be shown that

$$\mathbf{D}_{01} = \mathbf{M}_1 \mathbf{K}_{01} \quad (21)$$

$$\mathbf{S}_0 = (\mathbf{K}_{01})^T \mathbf{M}_1 \mathbf{K}_{01} \quad (22)$$

$$\mathbf{D}_{12} = \mathbf{M}_2 \mathbf{K}_{12} \quad (23)$$

$$\mathbf{S}_1 = (\mathbf{K}_{12})^T \mathbf{M}_2 \mathbf{K}_{12} \quad (24)$$

$$\mathbf{D}_{23} = \mathbf{M}_3 \mathbf{K}_{23} \quad (25)$$

$$\mathbf{S}_2 = (\mathbf{K}_{23})^T \mathbf{M}_3 \mathbf{K}_{23} \quad (26)$$

where $\mathbf{K}_{p(p+1)}$ is a “topological derivative” matrix. This matrix is the discretization of the exterior derivative operator d from differential geometry, $dW^p = W^{(p+1)}$. This matrix depends upon the mesh connectivity, but is independent of the nodal coordinates. It does not involve an integral over the element, and it does not involve any material properties. While seemingly abstract, it is enormously valuable in practice. The FEMSTER library computes the topological derivative matrices \mathbf{K}_{01} , \mathbf{K}_{12} , and \mathbf{K}_{23} . Given a p -form quantity X with basis function expansion

$$X = \sum_{i=1}^n x_i W_i^p, \quad (27)$$

and a $(p + 1)$ -form quantity Y with basis function expansion

$$Y = \sum_{i=1}^n y_i W_i^{(p+1)}, \quad (28)$$

the exterior derivative (gradient, curl, divergence for $p = 0$, $p = 1$, and $p = 2$, respectively) is given by

$$\mathbf{y} = \mathbf{K}_{p(p+1)} \mathbf{x}. \quad (29)$$

It can be shown that

$$\mathbf{K}_{12} \mathbf{K}_{01} = 0 \quad (30)$$

$$\mathbf{K}_{23} \mathbf{K}_{12} = 0 \quad (31)$$

which are the discrete versions of the identities $\nabla \times \nabla F = 0$ and $\nabla \cdot \nabla \times F = 0$, respectively. These identities are satisfied in the discrete sense, exactly (well, to machine precision), for any mesh and any order basis function.

FEMSTER contains some additional miscellaneous functionality. In some circumstances it is necessary to convert a p -form to a $(3 - p)$ -form, i.e. a Hodge-star operation. A classic example is converting a "cell-center" quantity to a "nodal" quantity. In our finite element setting the Galerkin procedure prescribes rectangular matrices of the form

$$(\mathbf{H}_{p(3-p)})_{ij} = \int_{\Omega} W_i^p \wedge W_j^{(3-p)} d\Omega \quad (32)$$

which produces optimal (in the least-square error sense) Hodge-star operators for arbitrary order basis functions. FEMSTER also computes a variety of "load vectors" that are used as source terms in finite element discretizations,

$$\mathbf{f}_{0j} = \int_{\Omega} f W_j^0 d\Omega \quad (33)$$

$$\mathbf{f}_{1j} = \int_{\Omega} f \cdot W_j^1 d\Omega \quad (34)$$

$$\mathbf{f}_{2j} = \int_{\Omega} f \cdot W_j^2 d\Omega \quad (35)$$

$$\mathbf{f}_{3j} = \int_{\Omega} f \cdot W_j^3 d\Omega \quad (36)$$

$$\mathbf{g}_{0j} = \int_{\Gamma} g W_j^0 d\Gamma \quad (37)$$

$$\mathbf{g}_{1j} = \int_{\Gamma} g \cdot W_j^1 d\Gamma \quad (38)$$

$$\mathbf{g}_{2j} = \int_{\Gamma} g \cdot W_j^2 d\Gamma \quad (39)$$

4.2 FEM Discretization of the Wave Equation

For the electric field, current density and polarization variables, the discretization is in terms of the 1-form edge basis functions $W_i^1 \in \mathcal{H}(curl)$.

$$\mathbf{E} = \sum_{i=1}^{N_{edges}} e_i W_i^1 \quad (40)$$

$$\mathbf{J} = \sum_{i=1}^{N_{edges}} j_i W_i^1 \quad (41)$$

$$\mathbf{P} = \sum_{i=1}^{N_{edges}} p_i W_i^1 \quad (42)$$

The variational form of the second order electric field wave equation (2) is becomes (43).

$$\begin{aligned} & \frac{\partial^2}{\partial t^2}(\bar{\epsilon}\mathbf{E}, \mathbf{E}^*) + \frac{\partial}{\partial t}(\bar{\sigma}_E \mathbf{E}, \mathbf{E}^*) = \\ & -(\bar{\mu}^{-1} \nabla \times \mathbf{E}, \nabla \times \mathbf{E}^*) - \frac{\partial}{\partial t}(\mathbf{J}_s, \mathbf{E}^*) - \frac{\partial^2}{\partial t^2}(\mathbf{P}, \mathbf{E}^*) - \oint_{\Gamma} \bar{\mu}^{-1} (\mathbf{E}^* \times \nabla \times \mathbf{E}) \cdot \hat{n} \forall \mathbf{E}^* \in \mathcal{H}(curl) \end{aligned} \quad (43)$$

In this equation the notation $(\mathbf{E}, \mathbf{E}^*)$ represents an integral over the problem domain Ω and Γ represents the boundary of Ω .

Entering the expansions for the electric field and electric and magnetic current densities results in the second order electric wave equation (44).

$$\mathbf{M}_1(\bar{\epsilon}) \frac{\partial^2}{\partial t^2} e + \mathbf{M}_1(\bar{\sigma}_E) \frac{\partial}{\partial t} e = -\mathbf{S}_1(\bar{\mu}^{-1}) e - \mathbf{M}_1 \frac{\partial}{\partial t} j - \mathbf{M}_1 \frac{\partial^2}{\partial t^2} p - \oint_{\Gamma} (\bar{\mu}^{-1} W_j^1 \times \nabla \times \mathbf{E}) \cdot \hat{n} \quad (44)$$

The essential and natural boundary conditions can be determined from the boundary condition term in the variational equation (43). In this wave equation the essential boundary condition corresponds to the Dirichlet boundary condition and the natural boundary condition corresponds to the Neumann boundary condition (45)

$$\begin{aligned} \mathbf{E} \times \hat{n} &= D \text{ on } \Gamma_D \\ \nabla \times \mathbf{E} \times \hat{n} &= N \text{ on } \Gamma_N \end{aligned} \quad (45)$$

where Γ_D and Γ_N represent the portion of the domain boundary on which Dirichlet and Neumann boundary conditions are applied, respectively. The boundary term can be evaluated in terms of the discrete basis functions and is shown in (46). The resulting matrix is zero due to the choice of test space.

$$\oint_{\Gamma} \bar{\mu}^{-1} (\mathbf{E}^* \times \nabla \times \mathbf{E}) \cdot \hat{n} = (\bar{\mu}^{-1} \nabla \times W_i^1, W_j^1 \times \hat{n})_{\Gamma} = 0, W_j^1 \in \mathcal{H}(curl) \quad (46)$$

4.3 FEM Discretization of the Polarization Equations

In this section the finite-element discretizations for the auxiliary differential equation and rate equations implemented for the Polarization dynamics equations are derived. The discretization for the polarization equation will be based on (9). The polarization is expanded in terms of 1-form basis functions as shown in (42). The population density variables N_i can be expanded in terms of 0-form or 3-form basis functions. The proper discrete differential form for a density function is a 3-form or volume basis functions $W_i^3 \in L_2$ (47). In many instances 0-form versions of these variables are required and a hodge operation converting the 3-form to a 0-form is performed.

$$N = \sum_{i=1}^{N_{nodes}} n_i W_i^3 \quad (47)$$

The variational form of the second polarization equation (9) is shown (48).

$$\begin{aligned} \frac{d^2}{dt^2}(\mathbf{P}, \mathbf{P}^*) + \gamma \frac{d}{dt}(\mathbf{P}, \mathbf{P}^*) + \omega_a^2 \frac{d}{dt}(\mathbf{P}, \mathbf{P}^*) = \\ \zeta(\Delta N \wedge \mathbf{E}, \mathbf{P}^*) \forall \mathbf{P}^* \in \mathcal{H}(curl) \end{aligned} \quad (48)$$

Here the wedge product \wedge scales the electric field by ΔN . The result is a 1-form variable and can be treated as a scaled \mathbf{E} for the variational form. Entering the expansions for the electric field and electric and magnetic current densities results in the second order electric wave equation (49).

$$\frac{d^2}{dt^2} p + \gamma \frac{d}{dt} p + \omega_a^2 p = v(\Delta n \wedge e) \quad (49)$$

The wedge product is performed by first converting the 3-form population density variable N to a 3-form and then scaling the 1-form vector e by this value to obtain a 1-form vector source.

The discretization for the first method is identical. The variational form for a prototypical population density equation is shown in (50).

$$\frac{d}{dt}(N_2, N^*) = \frac{(N_3, N^*)}{\tau_{32}} - \frac{(N_2, N^*)}{\tau_2} + \frac{1}{\hbar \omega_a} (\mathbf{E}^* \wedge \frac{d}{dt} \mathbf{P}, N^*) \forall N^* \in L_2 \quad (50)$$

In this case the wedge product is discretized using cell centered values for \mathbf{E} and \mathbf{P} . The dot product of the two vector values is evaluated at all 3-form integration points and given to the solver as a 3-form vector. The discretized equation for a prototypical rate equation is shown in (51).

$$\frac{d}{dt} n_2 = \frac{n_3}{\tau_{32}} - \frac{n_2}{\tau_2} + \frac{1}{\hbar \omega_a} (e \wedge p)_3 \quad (51)$$

The time discretization for all of the equations above is purely explicit. The full set of equations for the one-electron model are shown in (52).

$$\begin{aligned} \frac{d}{dt} n_3 &= W_p - \frac{n_3}{\tau_3} \\ \frac{d}{dt} n_2 &= \frac{n_3}{\tau_{32}} - \frac{n_2}{\tau_2} + \frac{1}{\hbar \omega_a} (e \wedge p)_3 \\ \frac{d}{dt} n_1 &= \frac{n_3}{\tau_{31}} + \frac{n_2}{\tau_{21}} - \frac{n_1}{\tau_1} - \frac{1}{\hbar \omega_a} (e \wedge p)_3 \end{aligned} \quad (52)$$

References

- [1] S. H. Chang and A. Taflove, “Finite-difference time-domain model of lasing action in a four-level two-electron atomic model,” vol. 12, no. 16, pp. 3827–3833, 2004.
- [2] A. S. Nagra and R. A. York, “FDTD analysis of wave propagation in nonlinear and absorbing and gain media,” *IEEE Trans. Ant. Prop.*, vol. 46, no. 3, pp. 334–340, 1998.
- [3] P. Castillo, J. Koning, R. Rieben, M. Stowell, and D. White, “Discrete differential forms: A novel methodology for robust computational electromagnetics,” Tech. Rep. UCRL-ID-151522, Lawrence Livermore National Laboratory, Center for Applied Scientific Computing, January 2003.